

LONG-TERM X-RAY STABILITY AND UV VARIABILITY OF THE IONIZED ABSORPTION IN NGC 3783

A. E. SCOTT^{1,2}, W. N. BRANDT^{1,2}, E. BEHAR³, D. M. CRENSHAW⁴, J. R. GABEL⁵, R. R. GIBSON⁶,
S. KASPI³, S. B. KRAEMER⁷, T. J. TURNER⁸

¹Department of Astronomy & Astrophysics, 525 Davey Laboratory, Pennsylvania State University, University Park, PA 16802, USA; amyscott@psu.edu

²Institute for Gravitation and the Cosmos, Pennsylvania State University, University Park, PA 16802, USA

³Department of Physics, Technion, Haifa 32000, Israel

⁴Department of Physics and Astronomy, Georgia State University, 25 Park Place, Suite 605, Atlanta, GA 30303, USA

⁵Physics Department, Creighton University, Omaha, NE 68178, USA

⁶Department of Astronomy, University of Washington, Box 351580, Seattle, WA 98195, USA

⁷Institute for Astrophysics and Computational Sciences, Department of Physics, The Catholic University of America, Washington, DC 20064, USA

⁸Department of Physics, University of Maryland Baltimore County, 1000 Hilltop Circle, Baltimore, MD 21250, USA

Accepted 2014 October 15

ABSTRACT

We present the results of recent *Chandra* High-Energy Transmission Grating Spectrometer and *Hubble Space Telescope* Cosmic Origins Spectrograph observations of the nearby Seyfert 1 galaxy NGC 3783 which shows a strong, non-varying X-ray warm absorber and physically related and kinematically varying UV absorption. We compare our new observations to high-resolution, high signal-to-noise archival data from 2001, allowing a unique investigation into the long-term variations of the absorption over a 12 yr period. We find no statistically significant changes in the physical properties of the X-ray absorber, but there is a significant drop of $\sim 40\%$ in the UV and X-ray flux, and a significant flattening of the underlying X-ray power-law slope. Large kinematic changes are seen in the UV absorbers, possibly due to radial deceleration of the material. Similar behavior is not observed in the X-ray data, likely due to its lower velocity resolution, which shows an outflow velocity of $v_{\text{out}} \sim -655 \text{ km s}^{-1}$ in both epochs. The narrow iron $K\alpha$ emission line at 6.4 keV shows no variation between epochs, and its measured width places the material producing the line at a radial distance of $\sim 0.03 \text{ pc}$ from the central black hole.

Keywords: galaxies: active — galaxies: Seyfert — galaxies: individual (NGC 3783) — X-rays: galaxies

1. INTRODUCTION

There is increasing evidence that supermassive black holes (SMBHs) co-evolve with the bulges of their host galaxies. The tight correlation between the velocity dispersion of stars in the bulge and the mass of the black hole at the center ($M-\sigma$; e.g., Ferrarese & Merritt 2000; Gebhardt et al. 2000; Gültekin et al. 2009; McConnell & Ma 2013; Kormendy & Ho 2013), suggests regulatory feedback (e.g., Silk & Rees 1998; King 2003, 2005; McQuillin & McLaughlin 2013) from the Active Galactic Nucleus (AGN), likely in the form of jets or winds. Such winds give rise to blueshifted absorption lines seen in the UV spectra of approximately half of Seyfert galaxies (e.g., Crenshaw et al. 1999), commonly the same AGN which also show a ‘warm absorber’ (WA; Halpern 1984) in their soft X-ray spectra (e.g., Reynolds 1997). This, along with the similarity of the outflow velocities inferred, suggests that the UV and X-ray absorbers are at least partly related physically and may be different manifestations of the same outflow (e.g., Mathur et al. 1994; Shields & Hamann 1997; Crenshaw et al. 1999).

Despite their importance and prevalence, the properties of these AGN winds are still not fully understood and their origin within the AGN structure is unclear. Two main scenarios suggest that the winds responsible for the warm absorber features are produced at very different locations. Krolik & Kriss (2001) propose that a multi-temperature wind is formed from photoionized evaporation of material off the inner edge of the torus located at parsec-scales from the central SMBH. However, Elvis (2000) suggests that a wind emerges vertically from a narrow region on the accretion disk at $\sim 1000 R_g$ (corresponding to $5 \times 10^{-4} \text{ pc}$ for a $10^7 M_\odot$ black hole) and is ra-

dially accelerated by radiation pressure and bent to an angle of $\sim 60^\circ$. Such a wind may produce the signature of a warm absorber at pc-scales when it collides with the shell of gas that has been swept up by radiation pressure and surrounds the black hole at 1–100 pc (King & Pounds 2014).

Determining the radial distance of the absorbing material from the central SMBH is therefore crucial for understanding its origin within the AGN structure. However, this quantity is not directly measurable (see e.g., Crenshaw & Kraemer 2012). Since the thickness of the absorber cannot exceed its distance from the SMBH an absolute maximum distance can be determined ($r_{\text{max}} \leq L_{\text{ion}}/\xi N_{\text{H}}$; Turner et al. 1993). A minimum can be estimated from the size of the C IV broad-line region as this is always at least partially covered (e.g., Crenshaw & Kraemer 2012) or by assuming the outflow is travelling at the local escape velocity (e.g., Tombesi et al. 2013). More stringent limits can be obtained from absorption of excited states (e.g., Kaastra et al. 2004) or from variability of the absorption. In particular, if the absorbers do not respond to changes in the ionizing continuum, an upper limit on the density of the absorber is obtained, giving a lower limit on its radial distance.

Variability has been observed previously in WA; indeed, the first WA was identified after an apparent increase in the absorption column density (N_{H}) occurred over $\sim 1 \text{ yr}$ in MR 2251-178 (Halpern 1984; Pan et al. 1990). Further observations with *ASCA* showed variations in N_{H} and the ionization parameter (ξ) on timescales of months to yrs, which were explained by material moving in and out of the line-of-sight (Kaspi et al. 2004). However, absorption in this AGN has also been observed to remain stable over a period of $\sim 9 \text{ yrs}$ since 2002 (Reeves et al. 2013). There are many other exam-

ples of AGN whose WA show variability, covering a range of timescales. For example, short timescale absorption variability was observed in MCG-6-30-15, with a factor of 2 increase in N_{H} seen over a period of 3 weeks (Fabian et al. 1994), changes in individual absorption lines have been observed over days (Gibson et al. 2007), and occultation events have been observed to occur over $\lesssim 8$ hrs (McKernan & Yaqoob 1998; Marinucci et al. 2014). Longer timescale variability is observed in Mrk 348, with a decrease in N_{H} and ξ in some of its absorption components occurring over 6 yrs (Marchese et al. 2014), and Mrk 704 shows very large changes (up to factors of ~ 8 depending upon which spectral model is adopted) in the covering factor, f , N_{H} , and ξ over 3 yrs (Matt et al. 2011). Similarly, Longinotti et al. (2013) report the re-emergence of a WA in Mrk 335 after $\gtrsim 10$ yrs of observations in which no absorption was detected, indicating both large and long-term variations. NGC 3516 shows absorption which is variable over a range of timescales with an occultation occurring over hours (Turner et al. 2008), changes in ionization state occurring over months (Turner et al. 2005) and the appearance of fast kinematic components happening after years (Holczer & Behar 2012). However, similar to MR 2251-178, other AGN show periods in which their WA do not appear to vary; e.g., NGC 5548 has shown periods of 3 yrs (1999–2002) with no apparent change in its properties (Steenbrugge et al. 2005), but others (2002–2005) do show a decrease in the ionization (Detmers et al. 2008). Later monitoring of this AGN in 2007 with *Suzaku* over month-timescales again shows the WA properties to be stable, despite large variations in the continuum flux (Krongold et al. 2010). Recent monitoring with *XMM-Newton* during 2013 shows the nucleus of NGC 5548 to be obscured by a long-lasting, clumpy stream of ionized gas, thus leading to a further change in the X-ray absorption (Kaastra et al. 2014). The absorption components in Mrk 509 do not show short-term variation over a monitoring period of 36 days, despite an increase in soft X-ray flux of 60% during the campaign. No long-term (3 to 9 yrs) changes are detected either, suggesting the absorbing material lies at large ($> \text{pc}$) distances from the black hole (Kaastra et al. 2012). Intrinsic UV absorption has also been observed to vary in many sources, due to changes in the ionization state of the material or motion of material across the line of sight giving a variable column density (e.g., Maran et al. 1996; Shields & Hamann 1997; Kraemer et al. 2001, 2002).

NGC 3783 is a nearby ($z = 0.00976 \pm 0.00009$; de Vaucouleurs et al. 1991), optically bright ($V \simeq 13$ mag) Seyfert 1 with a black hole mass of $M_{\text{BH}} = (2.98 \pm 0.54) \times 10^7 M_{\odot}$ (Peterson et al. 2004). It has been studied extensively in the X-ray band and has a strong X-ray warm absorber (e.g., Turner et al. 1993; George et al. 1998; De Rosa et al. 2002; Kaspi et al. 2000, 2001, 2002; Blustin et al. 2002; Behar et al. 2003; Brenneman et al. 2011). The first high-resolution grating observations from *Chandra* showed many blueshifted, narrow absorption lines from hydrogen- and helium-like ions of Ar, S, Si, Mg, Ne, and O, and L-shell transitions of Fe XVII to Fe XXI as well as weak emission lines from O and Ne (Kaspi et al. 2000). Further photoionization calculations indicated these were due to two phases of gas with different covering factors and different ionization levels (Kaspi et al. 2001). Kaspi et al. (2002; hereafter K02) presented a high signal-to-noise (S/N), high-resolution X-ray spectrum from 900 ks of *Chandra* data obtained in 2001. Narrow absorption lines from Fe, Ca, Ar, S, Si, Al, Mg, Ne, O, N, and C were again identified, with an average outflow velocity of

$v_{\text{out}} = -590 \pm 150 \text{ km s}^{-1}$. The lines showed an asymmetry in their profiles, thought to be due to the two separate absorbing systems. Absorption lines from lower ionization state ions were also observed, along with M shell transitions of Fe. Global photoionization modelling of this data set by Netzer et al. (2003) found it to be best described by three distinct absorption components with a large range in ionization state ($\log U_{\text{OX}} = -2.4, -1.2, -0.6$)¹, but a narrower range in column density ($\log N_{\text{H}} = 21.9, 22.0, 22.3$), with each split into two kinematic components. However, the same data set was modelled by Krongold et al. (2003) using only a two-phase absorber ($\log U_{\text{OX}} = -2.8, -1.2$, $\log N_{\text{H}} = 21.6, 22.2$) and the same outflow velocity for each component ($v_{\text{out}} \sim 750 \text{ km s}^{-1}$). Similar models were found for *XMM-Newton* Reflection Grating Spectrometer (RGS; den Herder et al. 2001) data in which absorption lines from Fe, Ar, S, Si, Mg, Ne, O, N, and C were all identified. Two phases of gas, with $\log \xi = 2.4, 0.3$ ¹, $\log N_{\text{H}} = 22.45, 20.73$, and an outflow velocity of $\sim 800 \text{ km s}^{-1}$ were used (Blustin et al. 2002). Holczer et al. (2007) improved upon the traditional multi-component modelling by reconstructing a continuous distribution of column density with ionization parameter, also found in other Seyfert outflows (Behar 2009). No short-term variability of the absorption was found in either the *Chandra* or *XMM-Newton* data. The lack of response by the absorbers to changes in the continuum allowed lower distance limits of $r \geq 3.2, 0.6, 0.2 \text{ pc}$ to be placed on the components found in the *Chandra* data (Netzer et al. 2003), and $r \geq 0.5 \text{ pc}$ and $r \geq 2.8 \text{ pc}$ for the high and low ionization components identified in the *XMM-Newton* data (Behar et al. 2003). Longer timescale variations were observed with early *ASCA* data when the opacity of the WA decreased by a factor of ≈ 2 over an 18 month period (George et al. 1998). Changes in the ionization and column density may have also occurred in the 8 yrs between 2001 and a *Suzaku* observation in 2009 (Brenneman et al. 2011). The WA shows no signs of variability within this 210 ks observation (Reis et al. 2012).

NGC 3783 was the subject of an intensive monitoring campaign in the UV from 2000–2002. Combining 18 epochs from the Space Telescope Imaging Spectrograph (STIS; Woodgate et al. 1998) on board the *Hubble Space Telescope* (*HST*) and 5 epochs from the *Far Ultraviolet Spectroscopic Explorer* (*FUSE*), Gabel et al. (2003a; hereafter G03a) presented a high S/N spectrum covering 905–1730 Å. This showed blueshifted absorption from O VI, N V, C IV, N III, C III* and Ly α to Ly ϵ and the previously detected kinematic components with outflow velocities of -1320 km s^{-1} and -548 km s^{-1} (components 1 & 2; Maran et al. 1996; Crenshaw et al. 1999), -724 km s^{-1} (3; Kraemer et al. 2001), and -1027 km s^{-1} (4; Kaiser et al. 2002; Gabel et al. 2002). Gabel et al. (2003b; hereafter G03b) also found component 1 to be decelerating, and that the deceleration was increasing. This may be due to the directional shift of an absorber with respect to our line of sight or different regions of a continuous flow crossing our sightline. No decelerations were detected in the other kinematic components. Component 1 has also been shown to be composed of two distinct, but co-located regions (1a and 1b; Kraemer et al. 2001). Modelling by Gabel et al. (2005) found an ionization parameter of $\log U \sim -0.5$ ¹ for the

¹Although the conversions between different definitions of the ionization parameter depend upon the spectral energy distribution assumed for the source, approximate relations are: $\log U = \log \xi - 1.5$ (Crenshaw & Kraemer 2012) and $\log U = \log U_{\text{OX}} + 1.99$ (Krongold et al. 2003).

UV components 1b, 2, and 3, which is consistent with that of the lowest-ionization X-ray absorber and distances of the components were estimated to be $r_1 \sim 25$ pc, $r_2 \leq 25$ pc and $r_3 \leq 50$ pc.

The wealth of high S/N, high-resolution spectroscopy available for NGC 3783 has allowed a detailed characterization of its extremely rich X-ray absorption spectrum and UV absorbing material. Our aim is to extend the work of these studies and investigate the variability of the absorption to determine how the material evolves over long timescales. We therefore obtained a new 170 ks *Chandra* High-Energy Transmission Grating Spectrometer (HETGS; Markert et al. 1994) observation (taken in 2013) to compare with the 900 ks archival spectrum from 2001 in order to study the evolution of the absorbers over more than a decade at high-resolution. Previous high-resolution studies of NGC 3783 have only probed timescales of up to ~ 1 yr. We also obtained new *HST* Cosmic Origins Spectrograph (COS; Green et al. 2012) data taken within a few days of our X-ray observation to investigate similar long-term variation in the UV absorption, and further investigate the relationship between the X-ray and UV absorbers. A description of our X-ray and UV observations and data reduction is given in §2. We present our main analysis including an investigation of the broadband spectral shape, individual absorption lines and the kinematics of the absorbers in §3. We summarize our conclusions in §4.

2. OBSERVATIONS

2.1. *Chandra* data

NGC 3783 has been observed by *Chandra* (Weisskopf et al. 2000) once in 2000 and extensively in 2001, resulting in a combined exposure time of 888.1 ks. These data were originally reported in K02 and are re-analyzed here. In this work we also report results from two new *Chandra* observations taken in March 2013 with a combined exposure time of 160.7 ks. Details of all these observations are given in Table 1.

Table 1
Chandra observation log

Obsid	Seq No.	Start Time (UTD)	Exposure time (ks)
00373	700045	2000 Jan 20 23:33:16	56.4
02090	700280	2001 Feb 24 18:44:57	165.1
02091	700281	2001 Feb 27 09:17:51	168.9
02092	700282	2001 Mar 10 00:31:15	165.5
02093	700283	2001 Mar 31 03:36:27	166.1
02094	700284	2001 Jun 26 09:57:42	166.2
14991	702799	2013 Mar 25 16:49:21	59.0
15626	702799	2013 Mar 27 14:08:06	101.7

Chandra performed the observations with the HETGS (Markert et al. 1994), which consists of two separate gratings, the High Energy Grating (HEG) and the Medium Energy Grating (MEG), in the focal plane of the Advanced CCD Imaging Spectrometer (ACIS; Garmire et al. 2003) which images the resulting spectra. All 8 observations were reduced in a uniform and standard way using CIAO version 4.5 (Fruscione et al. 2006) and version 4.5.6 of the calibration database. The X-ray spectra were extracted for each grating arm, HEG and MEG, and for both the positive and negative first orders. Higher order spectra, which include $\leq 6\%$ of the counts in the first order, were not considered. Auxiliary response

files and redistribution matrices were generated using FULLGARF and MKGRMF respectively. The $\pm 1^{\text{st}}$ order spectra were combined using a weighted mean with weights $= 1/\sigma^2$ where $\sigma = 1 + \sqrt{N+0.75}$ (Gehrels 1986)² and N is the number of counts. The spectra from each of the 6 observations in 2000/2001 were combined (and hereafter will be referred to as the 2001 data). The two observations in 2013 were also combined and they did not show any significant differences before addition. HEG data in the wavelength range 1.25–13 Å were combined with MEG data in the range 1.7–26 Å, again using a weighted mean. The total number of counts in the resulting 0.5–10.0 keV combined spectra were 909,903 for the 2001 data and 73,762 for 2013. No background counts were subtracted in this analysis as their contribution is known to be small ($< 0.5\%$ of the signal in HETGS/ACIS). The spectra are corrected for a Galactic N_{H} contribution estimated to be $N_{\text{H}}^{\text{Gal}} = 1.4 \times 10^{21} \text{ cm}^{-2}$ using equation (7) in Willingale et al. (2013) and the values $E(B-V) = 0.12$ (Alloin et al. 1995) and $N_{\text{HI}} = 9.91 \times 10^{20} \text{ cm}^{-2}$ from the Leiden/Argentine/Bonn survey (LAB; Kalberla et al. 2005).

The top panel of Figure 1 shows the ‘fluxed’, $\pm 1^{\text{st}}$ order, combined HEG & MEG spectra for the 2001 data (black), and the 2013 data (red) plotted in the rest-frame of NGC 3783. The spectra are shown with a minimum bin size of 0.02 Å, which is twice the bin size used in subsequent analyses. The binning is also increased further where required, to ensure at least 10 counts per bin in the 2013 spectrum and 80 counts per bin in the 2001 spectrum. This improves the clarity of the figure, allowing the absorption and emission lines to be seen clearly (a more detailed view of individual absorption lines is given in Figure 4). The spectra do not show features resulting from the ACIS chip gaps, which would be wider than any of the spectral features we investigate.

2.2. *HST* data

NGC 3783 has been observed multiple times in the UV. In this work we present the most recent observation taken in March 2013 with COS (Green et al. 2012) on board *HST*. The observation was made within days of the recent *Chandra* observations described in the previous section. The observations were performed using the G130M and G160M gratings each with a resolving power of $\lambda/\Delta\lambda \simeq 16,000$ – $21,000$ and covering a wavelength range of 900–1450 Å and 1405–1775 Å respectively. The exposure time of the observation was 3.884 ks, as listed in Table 2.

Table 2
UV observations

Epoch	Date	Exposure Time (ks)	Instrument/ Grating
1 ^a	2000 Feb 27	5.400	STIS, E140M
2 ^a	2001 Feb – Apr	63.784	STIS, E140M
3 ^a	2002 Jan 06	4.942	STIS, E140M
4 ^b	2004 May 5	24.338	<i>FUSE</i>
5 ^b	2011 Mar 23	2.088	STIS, G430M
	2011 May 26	4.553	COS, G130M/G160M
6	2013 Mar 30	3.884	COS, G130M/G160M

Notes. ^aPresented in G03b. ^bEpochs to be presented in J. Gabel et al. (in preparation).

²In figures, the upper error is determined with $\sigma_+ = 1 + \sqrt{N+0.75}$ and the lower error with $\sigma_- = N - N(1 - \frac{1}{9N} - \frac{1}{3\sqrt{N}})^2$.

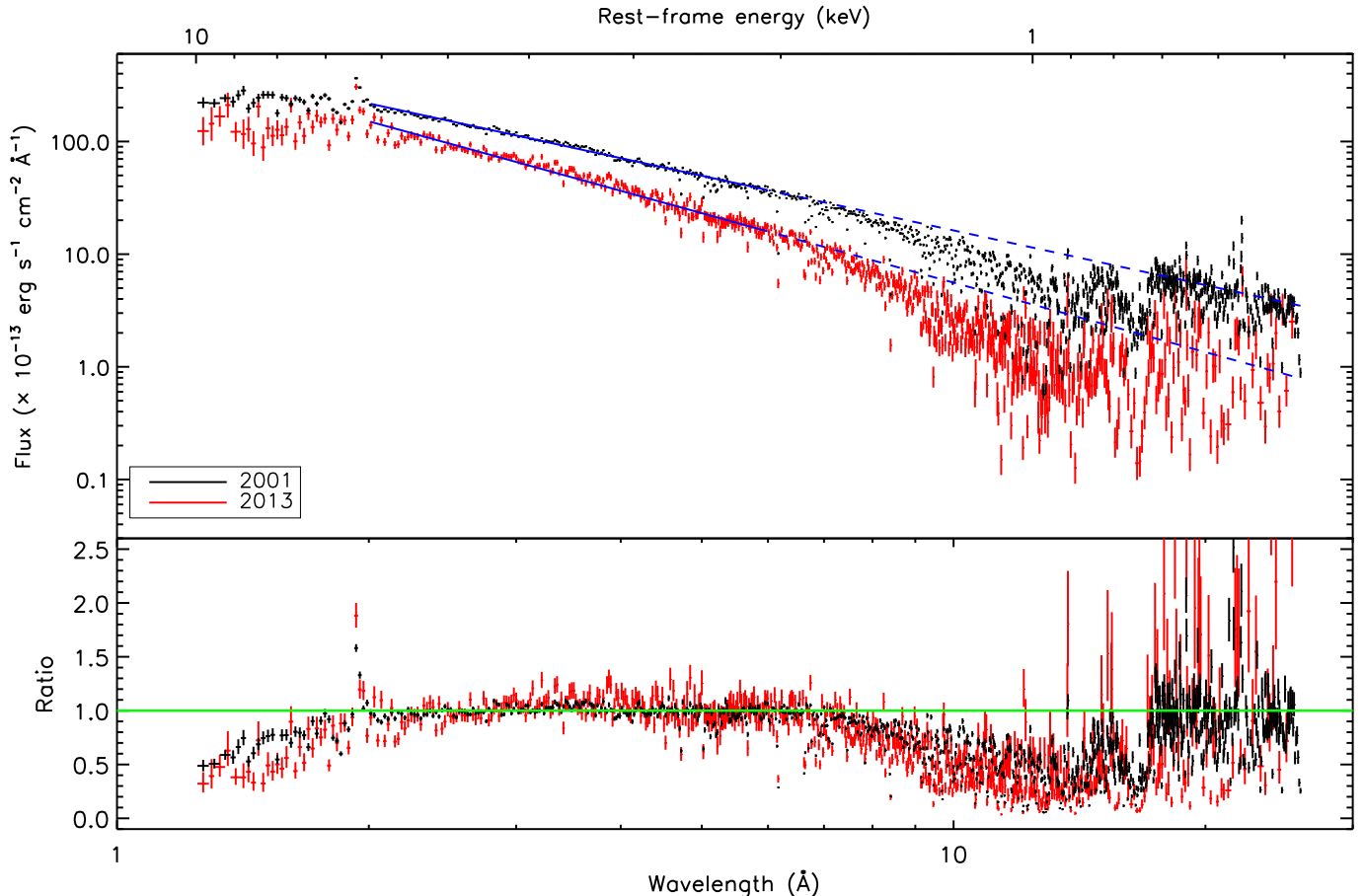


Figure 1. Broadband X-ray spectra of NGC 3783. Top - the combined HEG & MEG, $\pm 1^{\text{st}}$ order, fluxed spectra from the 2001 (black) and 2013 (red) observations. They are plotted with a minimum bin size of 0.02 \AA , which is increased as necessary so as to ensure at least 10 counts per bin in the 2013 spectrum, and 80 counts per bin for the 2001 spectrum. Shown in blue (solid) is the power-law fit to the data included in a Line Free Zone and within the wavelength range $2-6 \text{ \AA}$ ($\sim 2-6 \text{ keV}$). This fit is also shown extrapolated to longer wavelengths (blue, dashed). A more detailed view of each spectrum from $2-11 \text{ \AA}$ is given in Figure 4. Bottom - The ratio of the data to the power-law model shown in the top panel. The warm absorber at longer wavelengths/lower energies is clearly visible. The lower ratios at $\lambda < 2 \text{ \AA}$ are not caused by significant continuum absorption, but are a result of not modeling the reflection component in this figure. The spectra at $\lambda \gtrsim 11 \text{ \AA}$ show many emission lines, likely from the narrow-line region (NLR).

We also re-consider earlier *HST* data taken with STIS during the extensive monitoring campaign in 2001. These data were taken with the E140M medium-resolution echelle grating covering a wavelength range of $1144-1710 \text{ \AA}$ with a resolving power of $R \simeq 45,800$ and were originally reported in G03a (see that paper for more details on the data reduction). For consistency with G03b we refer to the UV observations by an ‘epoch number’ as listed in Table 2. In this work we consider observations from Epoch 2, as they most closely match the observation dates of the 2001 *Chandra* data. They have a combined exposure time of 63.784 ks . A *FUSE* spectrum from 2004 and *HST* spectra from 2011, listed as Epochs 4 & 5, will be discussed in J. Gabel et al. (in preparation). We refer to our most recent 2013 *HST* observation considered in this work as Epoch 6. Portions of the UV spectra are shown in Figure 2. Epoch 2 data from 2001 are shown in black, and Epoch 6 data from 2013 are shown in red.

3. RESULTS

3.1. Broadband spectra

In this section we assess changes in the broadband spectra of NGC 3783 between 2001 and 2013. Figure 1 shows the 2001 X-ray spectrum in black and the 2013 spectrum in red,

both corrected for Galactic N_{H} and plotted against rest-frame energy and rest-frame wavelength. We do not attempt a detailed modelling of the broadband continuum which is challenging due to the complexity of the warm absorber and possible presence of a soft X-ray excess and Compton reflection (e.g., De Rosa et al. 2002) for which we would require data at higher energies to constrain fully. Instead, we fit a power-law model to data in the range $2-6 \text{ \AA}$ ($\sim 2-6 \text{ keV}$) which is less affected by the absorption, allowing a simple comparison of the spectral shape in the two epochs. We also only include in the fitting those regions of the spectrum which do not contain strong absorption lines i.e., the Line Free Zones (LFZ) defined by Kaspi et al. (2001), although we note that few zones are entirely line free, and absorption edges still contribute to curvature in the spectrum. The best-fit parameters are not altered significantly when the all the data in the energy range, not just the LFZ, are used. The best-fitting model is shown in Figure 1 by the solid, blue line which is extrapolated to lower energies/longer wavelengths by the dashed, blue line. This figure clearly shows a drop in the X-ray flux between 2001 and 2013 and we measure $F_{2-6,2001} = (3.84 \pm 0.01) \times 10^{-11} \text{ erg s}^{-1} \text{ cm}^{-2}$ and $F_{2-6,2013} = (2.25 \pm 0.02) \times 10^{-11} \text{ erg s}^{-1} \text{ cm}^{-2}$ making the

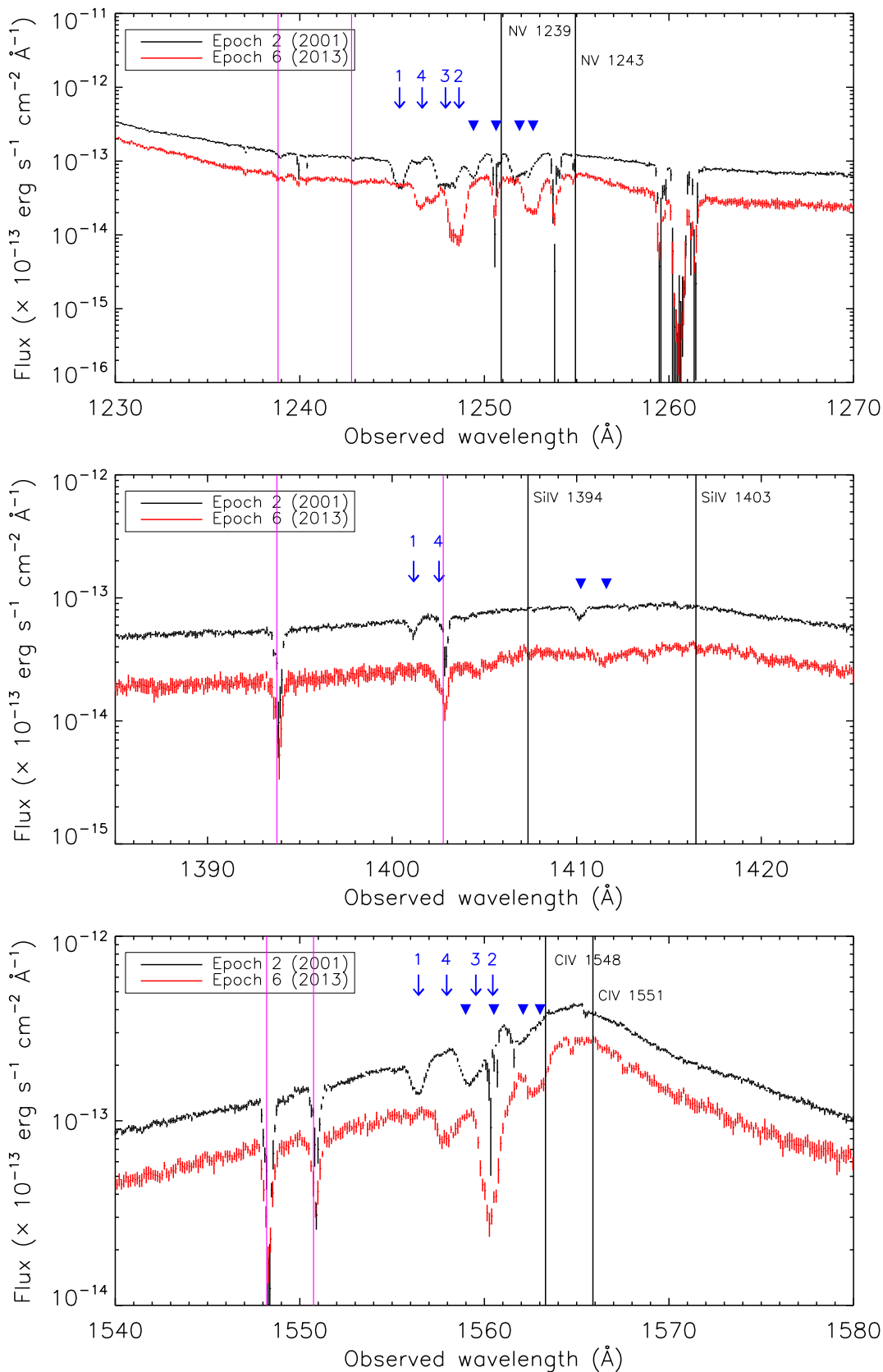


Figure 2. Sections of the UV spectra, clearly showing the drop in continuum flux between the two epochs and absorption troughs from the doublets of NV, SiIV and CIV. The data from Epoch 2 (2001) are shown in black, while the new 2013 observations of Epoch 6 are shown in red. Black vertical lines indicate the expected wavelength of the absorption lines in the rest-frame of NGC 3783 ($z = 0.00976$). The observed absorption troughs are noticeably blueshifted from these values and are highlighted with the blue arrows and triangles. Arrows indicate blueshifted absorption lines due to the shorter wavelength line in the doublet, while triangles indicate those due to the longer wavelength line. Numbers above the arrows refer to each of the UV kinematic components which are discussed in detail in Section 3.3.2. Note that not every component is present in both epochs. The vertical magenta lines identify Galactic interstellar absorption lines due to the ions shown in each respective panel. ISM lines due to other ions are also visible, but are not highlighted for clarity.

decrease highly significant³. We also see a significant flattening of the continuum slope, with $\Gamma_{2-6} = 1.37 \pm 0.01$ measured in the 2001 spectrum and $\Gamma_{2-6} = 1.07 \pm 0.04$ measured in 2013. Such variations in the power-law slope may be intrinsic, likely related to changes in the accretion flow close to the central SMBH, or they may be only apparent changes. These can be due to a change in the amount of absorbing material along the line-of-sight to the central source, or due to a change in the relative amounts of intrinsic and reflected emission contributing to the power-law observed. We comment on each of these possibilities below.

The bottom panel of Figure 1 shows the ratio of each spectrum to its 2–6 Å power-law model. This allows a simple comparison of the absorption at long wavelengths/low energies. The general shape appears similar in both epochs, suggesting no dramatic change in the warm absorbers. Although the narrow wavelength range (2–6 Å) over which we measure the power-law slope contains only a few strong absorption lines (e.g., from S between 3.5–5.4 Å), the warm absorber could still impact the continuum through bound-free absorption (see e.g., Figure 5 of Netzer et al. 2003; the Ca and Ar edges lie at 3.1 Å and 3.9 Å, respectively). We therefore measure the power-law slope over a series of progressively narrower wavelength ranges in order to estimate better the intrinsic continuum slope and determine whether the change in Γ between the two epochs is real, and not an artifact of increased absorption in 2013. For the 2001 spectrum we measure $\Gamma_{2-5\text{Å}} = 1.39 \pm 0.01$, increasing to $\Gamma_{2-4\text{Å}} = 1.44 \pm 0.02$ and $\Gamma_{2-3\text{Å}} = 1.47 \pm 0.05$. This shows an apparent convergence on $\Gamma \sim 1.47$ when more of the data thought to be contaminated by the spectral signature of the warm absorbers are excluded, indicating that they do affect shorter wavelengths/higher energies. Although this value is steeper as expected, it is still lower than the $\Gamma \sim 1.5-1.7$ often reported for NGC 3783 from models of the full spectrum (e.g., Blustin et al. 2002; Netzer et al. 2003; Krongold et al. 2003; Reeves et al. 2004). The power-law slope measured in the 2013 spectrum also steepens when a narrower energy range is used ($\Gamma_{2-5\text{Å}} = 1.13 \pm 0.05$, $\Gamma_{2-4\text{Å}} = 1.24 \pm 0.07$, and $\Gamma_{2-3\text{Å}} = 1.27 \pm 0.15$), but remains significantly flatter than in 2001, suggesting the observed change is real and unrelated to the warm absorbers. These fitting results are not affected by the wing of Fe K α .

The flattening of the power-law slope we see is consistent with the commonly observed Γ -flux relation for AGN (e.g., Taylor et al. 2003; Lamer et al. 2003; Pounds et al. 2004; Vaughan & Fabian 2004; Miller et al. 2007; Gibson & Brandt 2012) in that the slope flattens with a decrease in flux. This relation may be due to an increase in the fraction of the spectrum coming from reflection of the primary emission off some distant material, which only responds to a decrease in continuum flux after a time delay. We therefore model the 2001 spectra with a power-law plus neutral reflection model using $R = 0.9$ as found in *Suzaku* observations (Brenneman et al. 2011; Reynolds et al. 2012) and assume $E_{\text{cut}} = 200$ keV and $\cos i = 0.6$. We then simulate spectra with the best-fitting parameters from this model, but with only 60% of the power-law flux, consistent with the decrease previously observed. A simple power-law fit to these spectra over 2–6 Å gives $\Gamma = 1.34$. Although this is flatter than $\Gamma = 1.37$ which is observed in the 2001 data, it is not as flat as the value observed in 2013,

suggesting a fractional increase in the reflection component is unable to account for the change in power-law slope between the epochs. We also find that a stronger reflection component e.g., $R = 1.5$ is unable to explain the change in Γ within our data, which we note is not ideal for constraining a reflection component.

A study of SDSS quasars with multiple *Chandra* observations suggests that changes in the intrinsic power-law slope of $\Delta\Gamma = 0.3$ are not uncommon (Gibson & Brandt 2012) and similar, although smaller, spectral variations have been observed *within* previous observations of NGC 3783. For example, using *XMM-Newton* European Photon Imaging Camera (EPIC; Turner et al. 2001; Strüder et al. 2001) data, Reeves et al. (2004) observed a change in the power-law slope from $\Gamma = 1.57$ at low fluxes to $\Gamma = 1.71$ at high fluxes, consistent with the flux- Γ correlation, and the spectral variability observed in *BeppoSAX* observations was also explained with a small change of $\Delta\Gamma = 0.1$ in the power-law slope (De Rosa et al. 2002). *Suzaku* data also showed spectral variability on both short (20 ks) and longer (100 ks) timescales due to the central source, not the WA (Reis et al. 2012).

Long-term *Rossi X-ray Timing Explorer (RXTE)* monitoring of NGC 3783 shows considerable X-ray continuum variations on all timescales (e.g., Markowitz & Edelson 2004), with 2–10 keV flux changes as large as $\Delta F \sim 5 \times 10^{-11}$ erg s⁻¹ cm⁻² occurring over ~ 20 days. Such changes are consistent with our observations, and while some may be due to absorbing material, for example the occultation event found recently by Markowitz et al. (2014), others are more likely related to intrinsic variations within the X-ray continuum emitting region than persistent, rapid changes in the absorption. Figure 3 shows the long-term 2–10 keV X-ray light-curve for NGC 3783. The black data come from *RXTE* monitoring (Rivers et al. 2013), red tick marks indicate dates of *HST* observations, and colored symbols show X-ray fluxes from observations by other missions, including the magenta crosses which correspond to each of the *Chandra* observations presented in this work.

Figure 2 shows broad sections of the UV spectra; Epoch 2 data (2001) are shown in black, and Epoch 6 data (2013) are shown in red. It shows a drop in the continuum flux similar to that seen in the X-ray band with the average 1270–1520 Å flux in Epoch 6 being $40 \pm 4\%$ of the average Epoch 2 flux over the same wavelength range. Similarly to the X-ray continuum, the UV continuum is known to be highly variable (e.g., Reichert et al. 1994). Also shown are absorption features due to the doublets of N v ($\lambda\lambda$ 1238.821 Å, 1242.804 Å), Si iv ($\lambda\lambda$ 1393.76 Å, 1402.77 Å) and C iv ($\lambda\lambda$ 1548.202 Å, 1550.774 Å). Black vertical lines indicate the expected wavelengths of these absorption lines in the rest frame of NGC 3783, and the absorption profiles observed are blueshifted with respect to these positions, indicating the material is outflowing. The absorption troughs due to the shorter wavelength member of the doublet are highlighted by the blue arrows, and those due to the longer wavelength line are shown with solid blue triangles. The numbers shown above the arrows correspond to different kinematic components. These will be discussed in detail in §3.3.2, in which we present velocity profiles of the spectra in order to investigate further the outflow kinematics.

3.2. Individual absorption lines

The 900 ks X-ray spectrum taken in 2001 shows 135 narrow absorption lines from hydrogen-like, helium-like and lower-

³We also estimate $F_{2-10\text{keV},2001} = (5.55 \pm 0.03) \times 10^{-11}$ erg s⁻¹ cm⁻² and $F_{2-10\text{keV},2013} = (3.20 \pm 0.05) \times 10^{-11}$ erg s⁻¹ cm⁻², corresponding to a drop in flux of $42 \pm 1\%$.

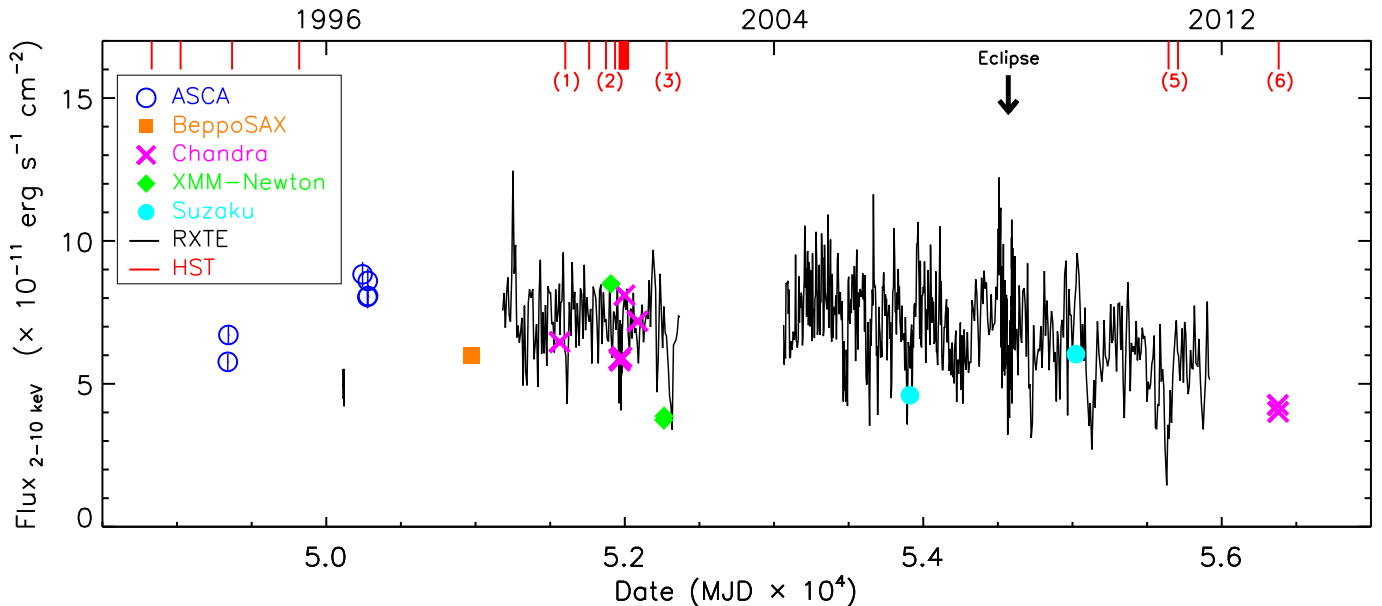


Figure 3. Long-term X-ray lightcurve for NGC 3783. The black line indicates the 2–10 keV flux determined from *RXTE* data (Rivers et al. 2013), which show a factor of 5 change in flux. The black arrow indicates the date of the apparent eclipse event found in the *RXTE* data by Markowitz et al. (2014). Colored symbols indicate the 2–10 keV flux from observations by other X-ray missions. They include *ASCA* (blue, open circles; George et al. 1998), *BeppoSAX* (orange square; De Rosa et al. 2002), *XMM-Newton* (green diamonds; Blustin et al. 2002, Reeves et al. 2004), *Suzaku* (cyan, filled circles; Miyazawa et al. 2009, Brenneman et al. 2011), and *Chandra* (magenta crosses; this work). These fluxes are determined from a simple power-law fit to the spectra from each individual *Chandra* observation used in this work. Note that Obsids 02090 and 02091 lie very close together on this figure. The dates of *HST* observations are indicated by the red tick marks at the top of the figure. The numbers in brackets refer to the epoch numbers listed in Table 2. Data from *HEAO-1* (Mushotzky et al. 1980), *EXOSAT* (Turner & Pounds 1989), and *Ginga* (Nandra & Pounds 1994) are also consistent with the range of fluxes shown in the figure, but are not included for clarity.

ionization ions of Fe, Ca, Ar, S, Si, Al, Mg, Ne, O, N, and C, including 1s–2p, and many higher order (e.g., up to 5p) transitions (K02; this work). Many of these absorption lines are also seen in the 2013 spectrum, although due to its lower S/N (9 at 7 Å compared with 37 at 7 Å in 2001) only those with the highest equivalent widths (EW) are detected with a high level of significance. However, these still originate from a range of ionization species and different order transitions. We look for changes in the absorption lines between epochs, which may be indicative of variations in the ionization state, column density, or line-of-sight covering factor of the absorbing material.

In this section we only consider the spectra up to a wavelength of 11 Å to ensure a good number of counts per bin while being able to maintain a bin size of $\Delta\lambda = 0.01$ Å required for the identification of the absorption lines. The 2001 spectrum contains at least 100 counts per bin throughout this wavelength range, while the 2013 spectrum contains > 10 counts per bin except for a few at longer wavelengths at the locations of absorption lines (the total number of counts included in each of the individual lines we consider in detail is > 80).

The spectra from both epochs are individually modelled with a power law to give a representation of the source continuum. We do not use a global power law fit to the full 2–11 Å spectrum as this does not give a good representation of the continuum due to the spectral curvature caused by absorption edges. As our data are not well suited to a detailed modelling of the continuum, in this analysis we simply model the continuum to a level such that we can investigate variations of the individual absorption lines. We do this using narrow wavelength ranges ($\Delta\lambda = 3$ Å) corresponding to those shown in each panel of Figure 4, over which the continuum is approximately a simple power-law. We also only include

data in the LFZ. At longer wavelengths not enough data remain in the LFZ to give a reliable fit. Therefore, in order to model the 8–11 Å range we extrapolate the power law fitted to data within 6–9 Å. We therefore caution that the continuum modelling in the > 9 Å region may not be optimal but we find no substantial changes to our results when we use the alternative data range of 5–9 Å in the fit. We estimate a 1σ error on the continuum level by considering the distribution of residuals about the resulting best-fit power-law. We note that the subsequent modelling of the individual absorption lines is dependent on the continuum used.

In order to assess any changes in the depths of the absorption lines between epochs, we plot the ratio of the data to the continuum fit in Figure 4. The 2001 data are shown in black, and the 2013 data are shown in red. The bottom panel of each sub-plot shows N_σ defined as

$$N_\sigma = \frac{R_{2013} - R_{2001}}{\sqrt{\sigma_{2013}^2 + \sigma_{2001}^2}}, \quad (1)$$

where R_{2013} and R_{2001} are the two ratios and σ_{2013} and σ_{2001} are their errors (Filiz Ak et al. 2013). This indicator allows a simple, visual indication of any potential changes between epochs. It is expected to lie between $\pm 1\sigma$ if the two spectra are not significantly different in that particular bin, with significant changes having $|N_\sigma| > 3$ (these levels are indicated by the dashed green lines). Even with no real variations in the absorption lines between the epochs, we still expect to see N_σ values at $> 1\sigma$ from purely statistical considerations. The N_σ values are expected to follow a Gaussian distribution, therefore of the 300 bins within any 3 Å segment, at least 95 are expected to have $|N_\sigma| > 1$, 14 will have $|N_\sigma| > 2$ and 1 will have $|N_\sigma| > 3$, regardless of any true variations of the absorption lines between epochs. However, due to the lower

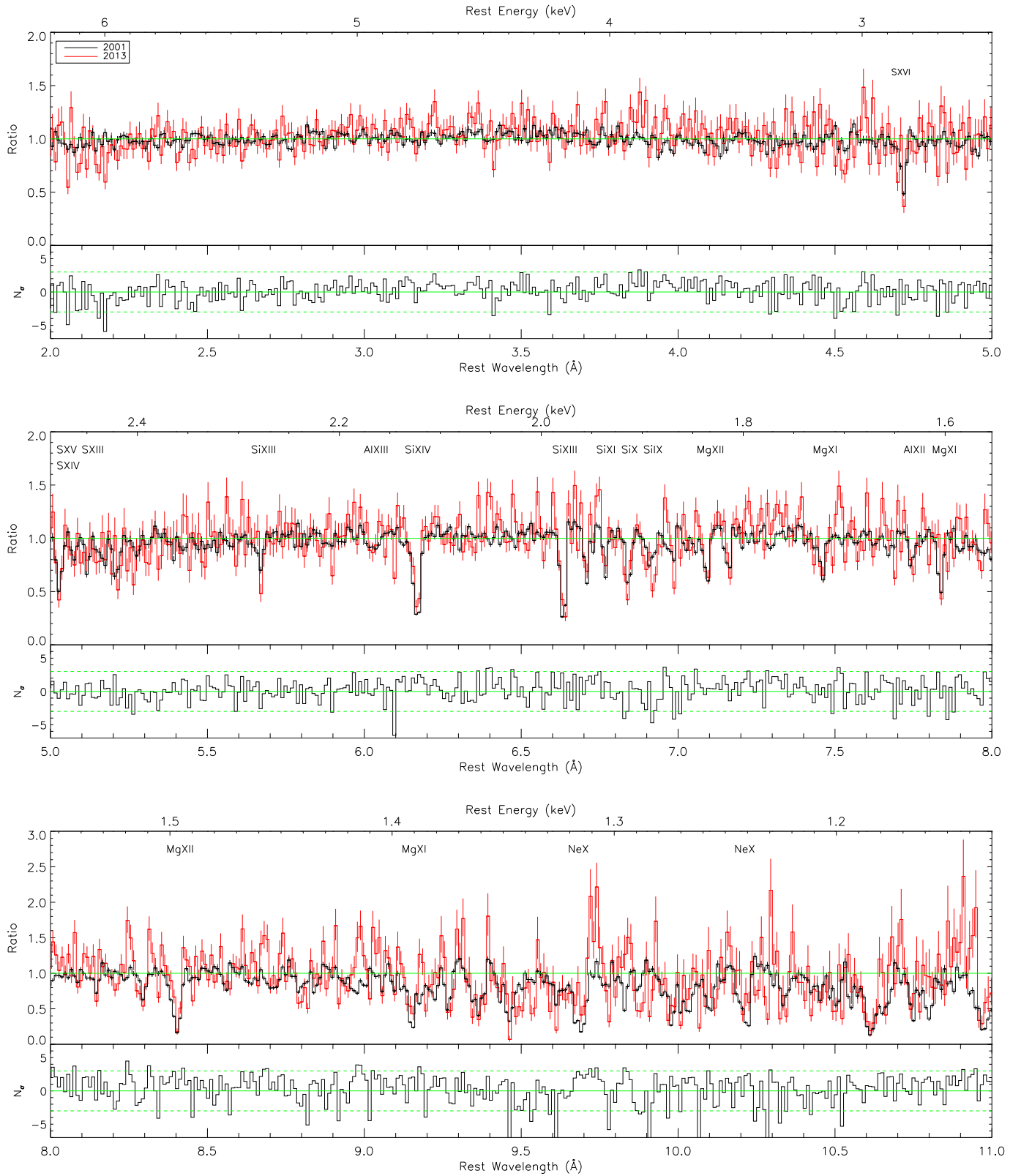


Figure 4. A comparison of the absorption lines in the spectra from both epochs. The top panels plot the ratios of the spectra divided by the continuum, which is modelled with a power law over the narrow wavelength range included in each panel (except for the 8–11 Å panel in which the continuum model is taken from a fit to the data in LFZ within 6–9 Å). The 2001 data are shown in black and the 2013 data are shown in red, both with 1σ error bars, and are plotted against rest-frame wavelength and rest-frame energy. The bottom panels show N_σ which is expected to lie between ± 1 if there is no significant variation between the two epochs. The dashed green lines show $|N_\sigma| = 3$ outside of which the spectra are significantly different in that bin. Strong, unblended absorption lines for which individual Gaussian fitting is carried out are labelled on the figure. We caution that emission lines appear artificially enlarged in this ratio plot due to their additive, rather than multiplicative nature.

S/N of the 2013 spectrum which affects the continuum modelling, there are many individual bins which display a significant variation ($> 3\sigma$). These features are not due to chip gaps which would produce features wider than the individual bin size. The positions of the main absorption lines we consider are labelled on Figure 4, and each typically covers 3–4 of the 0.01 \AA bins. In some cases N_σ indicates a significant variation in some, but not all of the bins within a line. We therefore instead use Gaussian fitting of the individual absorption lines which is more informative for assessing line variations.

We attempt to model each of the S, Si, Al, Mg, and Ne absorption lines that are listed as unblended by K02 with a Gaussian profile. The lines for which a Gaussian offers a good fit to the data are listed in Table 3 along with their transition (obtained from NIST⁴) and rest-frame wavelength. They are also labelled on Figure 4. In general, the line parameters we obtain for the 2001 spectrum are similar to those presented in K02. We note that more detailed analysis of the line profiles (see e.g., K02) indicates that they are not strictly Gaussian and have an asymmetry caused by material with different outflow velocities (see §3.3). However, assuming a Gaussian model is adequate for our purposes here, in which we compare line flux estimates to assess whether a particular absorption line has varied significantly in strength between epochs. For all lines we fit a Gaussian profile to the 2001 data in which all parameters are free to vary, and then fit the same Gaussian shape to the 2013 data; i.e., we fix the mean and sigma values, and allow only the line flux to vary. This allows us to determine whether the absorption line becomes stronger or weaker in the new data, assuming that the line profile does not change. These values are listed in Table 3 as the ‘2013 (fix)’ model. In some cases we are also able to fit a freely varying Gaussian profile to the lines in the new data (listed in Table 3 as ‘2013’), with λ_{obs} , σ , velocity shift and line flux being determined from the best-fitting Gaussian parameters. The full-width at half-maximum (FWHM) is determined from

$$\text{FWHM (km s}^{-1}\text{)} = 2\sqrt{2\ln 2} \left(\frac{\sigma c}{\lambda_{\text{obs}}} \right), \quad (2)$$

where σ and λ_{obs} are in units of \AA , and c is in km s^{-1} . In cases where the observed absorption line is thought to be comprised of a doublet, the velocity shift quoted is calculated with respect to the line of shortest wavelength. In Table 3 we list the physical line fluxes of the absorption lines in the 2013 spectra, and also quote a value which has been scaled using a factor determined from the ratio of the continua from both epochs at the line position (C_{2001}/C_{2013}). This removes the difference introduced by the lower continuum flux level of the 2013 data and allows a direct comparison of the line fluxes in each epoch. The significance of each change in σ units, is listed.

Of the 19 absorption lines we consider, 5 have a line flux which appears to vary significantly ($> 3\sigma$) between 2001 and 2013. For 3 of these, the absorption lines appear to be weaker in the 2013 data while maintaining a similar profile shape. These are the $1s - 2p$ transition of H-like Si XIV at a rest-frame wavelength of 6.182 \AA , the $1s - 2p$ transition of He-like Mg XI at $\lambda_{\text{rest}} = 9.169 \text{ \AA}$, and the $1s - 4p$ transition of H-like Ne X at $\lambda_{\text{rest}} = 9.708 \text{ \AA}$. However, in the original modelling of these lines, the level of the continuum was fixed to its best-fitting value. Therefore the errors on the line parameters listed in Table 3 are statistical errors only, and do not include

a contribution from the systematic error resulting from the uncertainty in the continuum placement. When the continuum level is allowed to vary within its 1σ error bounds, the measured differences in the line flux between the two epochs are no longer significant for each of the 3 lines ($\leq 1.6\sigma$).

The remaining two of the 19 lines show a change in their profile shape. The C-like, Si IX doublet at $\lambda_{\text{rest}} = 6.923, 6.939 \text{ \AA}$ appears as a single line in the 2001 spectrum, but as two separate lines in the 2013 spectrum. This prevents a direct comparison between the epochs, and since we only model the data with a single Gaussian, an apparent increase in the line flux is obtained. In the 2001 spectrum, the H-like, Mg XII absorption line at $\lambda_{\text{rest}} = 8.421 \text{ \AA}$ has a broad Gaussian profile with a FWHM of $1128 \pm 31 \text{ km s}^{-1}$, but in the 2013 spectrum the line is significantly narrower (5σ) with $\text{FWHM} = 662 \pm 83 \text{ km s}^{-1}$. This results in a significant change in the line flux, despite the deepest point of the line being consistent between epochs, in both position and depth. We allowed the continuum level to vary in additional Gaussian fits to this line, since the shape of the profile can also vary when a different continuum level is used. The variation of the FWHM is still significant between epochs (3.6σ), however, we note that this line is likely not resolved in the 2013 spectrum. We show an enlarged portion of the data in Figure 5 including the Gaussian fitting to this line as an example.

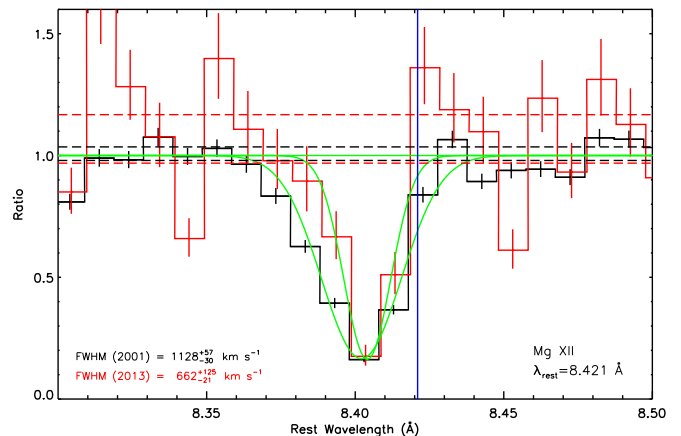


Figure 5. The Gaussian fitting of the Mg XII absorption line at $\lambda_{\text{rest}} = 8.421 \text{ \AA}$. The 2001 data are shown in black and the 2013 data are shown in red. A small artificial x offset of $+0.0005 \text{ \AA}$ has been added to the 2013 data to improve the clarity of the figure by reducing symbol overlap. The vertical blue line indicates λ_{rest} from which the absorption line is noticeably blueshifted. The best-fitting Gaussian profiles are shown in green and the parameters of the Gaussian fit to the 2013 data were left free to vary. The shape of the line profile is significantly narrower in the 2013 spectrum, even after accounting for the error on the continuum placement. The 1σ error bounds on the continuum level are indicated with the dashed black and red lines. The FWHM values quoted on the figure also include the systematic error associated with the continuum placement and therefore differ from those in Table 3, in which we list only the statistical errors.

In addition to comparing line fluxes derived from the Gaussian modelling, we also compare the EWs of the lines. For consistency with the previous work of K02 we derive this directly from the residuals, rather than the Gaussian fit. The EW is given by

$$\text{EW} = \sum_i \left(1 - \frac{F_i}{F_C} \right) B_i, \quad (3)$$

where F_i is the flux in the i th bin, F_C is the continuum level at that bin, and B_i is the bin width (0.01 \AA). The limits of sum-

⁴http://physics.nist.gov/PhysRefData/ASD/lines_form.html

Table 3
Parameters of the Gaussian fits to the strongest, unblended absorption lines.

Species (λ_{rest})	Data/ Model	λ_{obs} (\AA)	σ (m\AA)	FWHM (km s^{-1})	v_{shift} (km s^{-1})	Line flux ($\times 10^{-7}$ ph cm^{-2} s^{-1})		EW (m\AA)
						Physical	Scaled	
S XVI (4.729) (H-like, 1s – 2p)	2001	4.7181 ± 0.0006	8.0 ± 0.5	1198 ± 81	-691 ± 39	138.8 ± 8.8		10.8 ± 1.9
	2013 (fix)	76.9 ± 8.6	161.9 ± 18.2 (1.1 σ)	11.5 ± 5.0 (0.1 σ)
S XV (5.039) (He-like, 1s – 2p)	2001	5.0276 ± 0.0007	8.5 ± 0.6	1187 ± 89	-681 ± 39	139.2 ± 9.3		10.7 ± 2.2
	2013 (fix)	76.2 ± 10.7	154.0 ± 21.5 (0.6 σ)	7.2 ± 4.8 (0.7 σ)
	2013	5.027 ± 0.002	7 ± 2	1014 ± 217	-736 ± 116	68.3 ± 14.3	83.0 ± 46.0 (1.2 σ)	8.0 ± 5.7 (0.4 σ)
S XIV (5.084,5.086) (Li-like, 1s – 2p)	2001	5.074 ± 0.002	7 ± 1	1003 ± 207	-567 ± 103	48.7 ± 9.5		3.2 ± 2.6
	2013 (fix)	27.8 ± 13.0	56.8 ± 26.6 (0.3 σ)	6.7 ± 4.9 (0.6 σ)
S XIII (5.126) (Be-like, 1s – 2p)	2001	5.117 ± 0.001	6 ± 1	861 ± 134	-510 ± 60	71.7 ± 8.7		5.5 ± 2.0
	2013 (fix)	19.3 ± 12.1	39.6 ± 24.8 (1.2 σ)	4.3 ± 4.2 (0.3 σ)
	2013	5.106 ± 0.008	13 ± 9	1736 ± 1186	-1198 ± 450	40.4 ± 22.4	83.0 ± 46.0 (0.2 σ)	6.2 ± 5.9 (0.1 σ)
Si XIV (6.182) (H-like, 1s – 2p)	2001	6.1681 ± 0.0002	11.2 ± 0.3	1276 ± 34	-676 ± 12	233.1 ± 5.1		21.4 ± 2.6
	2013 (fix)	79.6 ± 5.6	192.4 ± 13.5 (2.8 σ)	14.5 ± 5.5 (1.1 σ)
	2013	6.1680 ± 0.0009	9 ± 1	976 ± 139	-677 ± 45	68.4 ± 7.4	165.3 ± 17.9 (3.6 σ)	14.5 ± 5.5 (1.1 σ)
Si XIII (6.648) (He-like, 1s – 2p)	2001	6.6340 ± 0.0002	7.7 ± 0.3	816 ± 32	-633 ± 8	161.6 ± 4.3		13.5 ± 2.5
	2013 (fix)	63.8 ± 3.6	164.2 ± 9.3 (0.3 σ)	11.6 ± 4.9 (0.3 σ)
Si XIII (5.681) (He-like, 1s – 3p)	2001	5.668 ± 0.001	8 ± 1	973 ± 129	-666 ± 60	67.0 ± 8.1		5.9 ± 2.5
	2013 (fix)	46.5 ± 8.8	104.5 ± 19.7 (1.8 σ)	5.4 ± 5.1 (0.1 σ)
Si XI (6.778) (Be-like, 1s – 2p)	2001	6.7678 ± 0.0009	4.9 ± 0.5	515 ± 54	-451 ± 39	46.1 ± 4.1		4.8 ± 1.4
	2013 (fix)	13.0 ± 4.0	34.0 ± 10.5 (1.1 σ)	3.1 ± 2.9 (0.5 σ)
Si X (6.854,6.864) (B-like, 1s – 2p)	2001	6.842 ± 0.0003	6.4 ± 0.6	662 ± 66	-508 ± 14	80.0 ± 4.2		8.4 ± 2.2
	2013 (fix)	38.4 ± 3.7	101.8 ± 9.9 (2.0 σ)	11.3 ± 4.0 (0.6 σ)
	2013	6.837 ± 0.001	8 ± 1	802 ± 135	-758 ± 61	42.3 ± 6.3	111.9 ± 16.6 (1.9 σ)	11.3 ± 4.0 (0.6 σ)
Si IX (6.923,6.939) (C-like, 1s – 2p)	2001	6.912 ± 0.001	10 ± 1	1058 ± 104	-497 ± 43	63.2 ± 5.3		5.6 ± 3.5
	2013 (fix)	44.3 ± 5.6	118.4 ± 15.0 (3.5 σ)	12.5 ± 5.7 (1.0 σ)
	2013	6.916 ± 0.003	15 ± 3	1547 ± 283	-302 ± 125	57.6 ± 9.0	153.9 ± 24.1 (3.7 σ)	15.2 ± 8.1 (1.1 σ)
Al XIII (6.053) (H-like 1s – 3p)	2001	6.029 ± 0.003	13 ± 3	1574 ± 354	-1197 ± 144	43.8 ± 8.9		3.0 ± 3.6
	2013 (fix)	12.1 ± 10.6	28.8 ± 25.1 (0.6 σ)	1.5 ± 2.5 (0.3 σ)
Al XII (7.757) (He-like 1s – 2p)	2001	7.7431 ± 0.0007	7 ± 1	608 ± 95	-537 ± 29	42.3 ± 4.3		5.2 ± 1.9
	2013 (fix)	17.7 ± 4.1	52.5 ± 12.1 (0.8 σ)	5.7 ± 3.7 (0.1 σ)
Mg XII (8.421) (H-like, 1s – 2p)	2001	8.4020 ± 0.0004	13.4 ± 0.4	1128 ± 31	-675 ± 12	217.1 ± 5.3		28.6 ± 2.6
	2013 (fix)	55.9 ± 3.1	194.8 ± 10.9 (1.8 σ)	10.2 ± 11.3 (1.6 σ)
	2013	8.404 ± 0.001	8 ± 1	662 ± 83	-603 ± 40	36.7 ± 4.3	128.0 ± 15.0 (5.6 σ)	14.1 ± 6.8 (2.0 σ)
Mg XII (7.106) (H-like, 1s – 3p)	2001	7.0921 ± 0.0004	6.0 ± 0.7	632 ± 69	-589 ± 18	69.5 ± 4.2		7.9 ± 1.8
	2013 (fix)	24.7 ± 3.9	67.4 ± 10.6 (0.2 σ)	6.9 ± 3.5 (0.3 σ)
Mg XI (9.169) (He-like, 1s – 2p)	2001	9.1543 ± 0.0006	18.9 ± 0.6	1454 ± 44	-480 ± 18	241.3 ± 6.5		35.3 ± 3.1
	2013 (fix)	41.2 ± 6.3	159.1 ± 24.2 (3.3 σ)	16.2 ± 13.7 (1.4 σ)
	2013	9.149 ± 0.003	12 ± 3	953 ± 222	-654 ± 82	34.6 ± 6.4	133.3 ± 24.6 (4.2 σ)	12.7 ± 10.1 (2.1 σ)
Mg XI (7.851) (He-like, 1s – 3p)	2001	7.8361 ± 0.0004	7.6 ± 0.5	685 ± 41	-569 ± 16	87.6 ± 4.2		9.7 ± 2.2
	2013 (fix)	29.4 ± 3.7	87.6 ± 11.0 (No change)	9.0 ± 4.4 (0.1 σ)
Mg XI (7.473) (He-like, 1s – 4p)	2001	7.4595 ± 0.0006	6.6 ± 0.6	622 ± 57	-543 ± 22	62.1 ± 4.2		7.7 ± 2.3
	2013 (fix)	21.0 ± 4.1	60.0 ± 11.6 (0.2 σ)	6.3 ± 4.5 (0.3 σ)
Ne X (9.708) (H-like, 1s – 4p)	2001	9.6857 ± 0.0005	20.9 ± 0.8	1523 ± 57	-690 ± 16	290.0 ± 8.5		41.9 ± 2.1
	2013 (fix)	43.0 ± 7.4	177.6 ± 30.5 (3.5 σ)	25.7 ± 10.4 (1.5 σ)
Ne X (10.239) (H-like, 1s – 3p)	2001	10.2185 ± 0.0004	11.2 ± 0.5	770 ± 37	-599 ± 11	184.9 ± 6.2		22.5 ± 2.9
	2013 (fix)	29.9 ± 5.6	131.8 ± 24.5 (2.1 σ)	18.7 ± 11.5 (0.3 σ)

Notes. In the ‘2013 (fix)’ model, the Gaussian shape is fixed to that used for the 2001 data, leaving only the line flux free to vary. For the 2013 data we quote both a physical line flux calculated directly from the data, and also a value that has been scaled using the ratio of the continuum fluxes in both epochs, to enable a direct comparison. The significance of the flux and EW changes between epochs for each line are listed in parentheses.

mation are taken as the points at which the Gaussian profile becomes indistinguishable from the continuum. The error is estimated by

$$\Delta EW = \sqrt{\left[\frac{\Delta F_C}{F_C} \sum_i \left(\frac{B_i F_i}{F_C} \right) \right]^2 + \sum_i \left(\frac{B_i \Delta F_i}{F_C} \right)^2}, \quad (4)$$

where ΔF_i is the error on the flux in the i th bin and ΔF_C is the error on the continuum level, estimated from the distribution of residuals about the best-fitting continuum level.

Unlike the original Gaussian modelling used to estimate the line fluxes, the EW determination directly includes an estimate of the error on the continuum. Using this criterion, none of the 19 individual absorption lines we consider show a significant change in EW between the two epochs. The results obtained from comparing the EW between epochs, and looking for changes in line flux, are therefore in good agreement. The significances of each change in EW, all of which are $\leq 2.1\sigma$, are listed in Table 3.

As none of the 19 absorption lines we investigate shows a significant variation between epochs considering both their line flux and EW, dramatic changes in the physical properties of the absorbing material are unlikely. However, our ability to detect significantly a variation in the line depends on the strength of the line itself (i.e., we might not significantly detect a change in a line that is weaker). We note that the 19 lines we consider are the strongest in the data set, despite covering a range of EW ($\sim 40 \text{ m}\text{\AA}$ to $\sim 3 \text{ m}\text{\AA}$), and therefore these lines represent the best chance of detecting variations. We estimate that for the Si XIV line ($\lambda_{\text{rest}} = 6.182 \text{ \AA}$), for example, we would be able to detect changes in the line flux of $\gtrsim 20\%$ and $\gtrsim 50\%$ at $> 1\sigma$ and $> 3\sigma$ significance, respectively; continuum placement uncertainty largely sets these lower bounds. However, photoionization modelling reported in Netzer et al. (2003) suggests that some of the strongest absorption lines may be saturated, and are therefore less sensitive to any changes in the column density. They include Si XIV (6.182 \AA), Si XIII (6.648 \AA), Si XIII (5.681 \AA), and S XVI (4.729 \AA), although S XV (5.039 \AA), Si XI (6.778 \AA), Si X (6.854 \AA), and Si IX (6.939 \AA) are thought to be unsaturated. Given the apparent lack of variation in the absorbing material, detailed photoionization modeling is not required. We find that the best-fitting model for the 2001 spectrum determined by Netzer et al. (2003), which includes the effects of three ionized absorbers, each split into two kinematic components, provides a good fit to the 2013 data, further indicating the constancy of the X-ray warm absorber.

With the exception of the Fe K α emission line which is considered in detail in §3.5, we do not investigate the properties of emission lines, many of which have $\lambda_{\text{rest}} > 11 \text{ \AA}$ where the S/N of the 2013 spectrum drops considerably. However, these emission lines are visible in Figure 1, and their contribution may be higher in the 2013 spectrum. This is due to the lower continuum flux level resulting in an increase in the relative contribution from the extended X-ray emission of the NLR. This increased emission could also cause apparent changes in the profiles of some absorption lines, and may explain the narrower shape of the Mg XII line we see. Figure 4 also shows a Ne emission line at $\lambda_{\text{rest}} = 9.708 \text{ \AA}$ (Ne X), which appears to be considerably stronger in the 2013 spectrum. However this is mostly an artifact of taking a ratio of the data and the additive, rather than multiplicative nature of emission lines, as the line fluxes in the two epochs are consistent at 1.6σ when the

error on the continuum placement is also considered.

3.3. Kinematics

3.3.1. X-ray kinematics

In this section we consider the stacking of multiple absorption lines from the same element in order to improve the statistics, and we do this in velocity space in order to probe the kinematics of the absorbing material directly. Our ‘velocity spectra’ are built up on a photon-by-photon basis using data directly from the event files rather than the spectra already binned in wavelength. Each event file is filtered, keeping events registered in the HEG or MEG and $\pm 1^{\text{st}}$ orders. Events from bad pixels are discarded and our results are not affected by spectral lines falling into ACIS chip gaps. The velocity shift of each photon is determined with respect to the expected wavelength of a number of different spectral lines. We consider each of the spectral lines listed by K02, excluding those which may be blended with lines from a different element. Lines from H-like and He-like ions of the same element are combined to give a larger number of photons in each bin. While no correlation between the ionization state and the blueshift of the lines was observed by K02, lower blueshifts were measured for increasing transition orders (e.g., 1s–3p, 4p, 5p). In our analysis we include lines from all transition orders which may result in a wider combined absorption profile. The velocity profiles for S, Si, Al, Mg, and Ne are shown in Figure 6. We do not show the profiles for Ca or Ar as they have a small average number of photons per bin and do not show a significant absorption profile. The individual lines included in each profile and their rest-frame wavelengths are listed on the figures. We also create a velocity profile by stacking *all* of the 23 H- and He-like absorption lines of S, Si, Al, Mg, and Ne resulting in a 2013 HEG profile with ~ 115 counts per bin and a 2013 MEG profile with ~ 250 counts per bin. These are shown in the top two panels of Figure 7. The left-hand panels in Figures 6 and 7 show profiles created from the HEG data, while the MEG profiles are shown on the right. The two grating arms are considered separately due to their different instrumental resolutions ($\Delta\lambda_{\text{HEG}} = 0.012 \text{ \AA}$, $\Delta\lambda_{\text{MEG}} = 0.023 \text{ \AA}$). The expected width of the profile created simply by the instrumental resolution is calculated from

$$\sigma_{\text{inst}} (\text{km s}^{-1}) = \left(\frac{\Delta\lambda}{\lambda} \right) \left(\frac{1}{2\sqrt{2\ln 2}} \right) c, \quad (5)$$

where λ is the shortest wavelength of any line included in the stacking to give an indication of the worst resolution expected. For each profile, the open-black circles show data from 2001 and the solid-red circles show data from 2013. Error bars are determined from the number of photons included in each velocity bin (Gehrels 1986), which have widths of 100 km s^{-1} . Each profile is divided by its own ‘continuum level’ (i.e., the typical number of photons in bins with $v < -2000 \text{ km s}^{-1}$ and $v > 0 \text{ km s}^{-1}$ which excludes the majority of the absorption profile), such that the profiles from each epoch are normalized to the same y-axis value of 1, allowing a direct comparison. The blue arrows indicate the velocity shifts of the four UV absorption components using the values listed in G03a. We also plot N_σ calculated from both the number of counts and the errors on each bin.

The velocity profiles shown in Figures 6 and 7 are modelled with a Gaussian plus a constant fixed at 1.0 by defi-

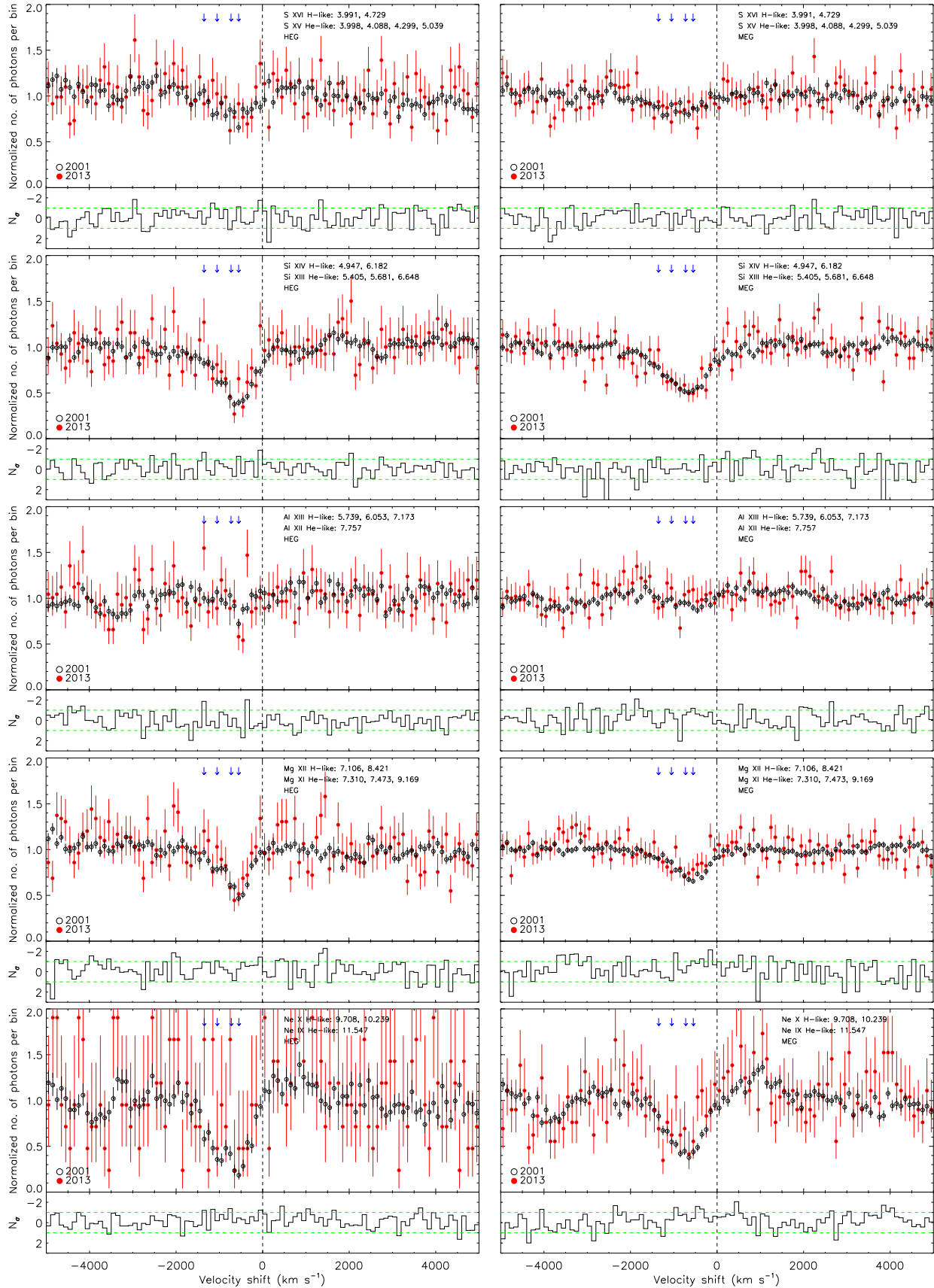


Figure 6. X-ray velocity profiles. The HEG (left) and MEG (right) velocity spectra are created by stacking absorption lines from H-like and He-like ions of the elements S, Si, Al, Mg, and Ne. Data from the 2001 observations are shown by the black-open circles, and data from the 2013 observations are shown by the red-solid circles. Error bars are computed from the number of counts included in each bin (Gehrels 1986). The bin size is 100 km s^{-1} . The rest-frame wavelengths of the individual absorption lines included in the profile are listed on each figure. The blue arrows indicate the locations of the four kinematic components identified in the UV spectra, using the velocity shift values from G03a.

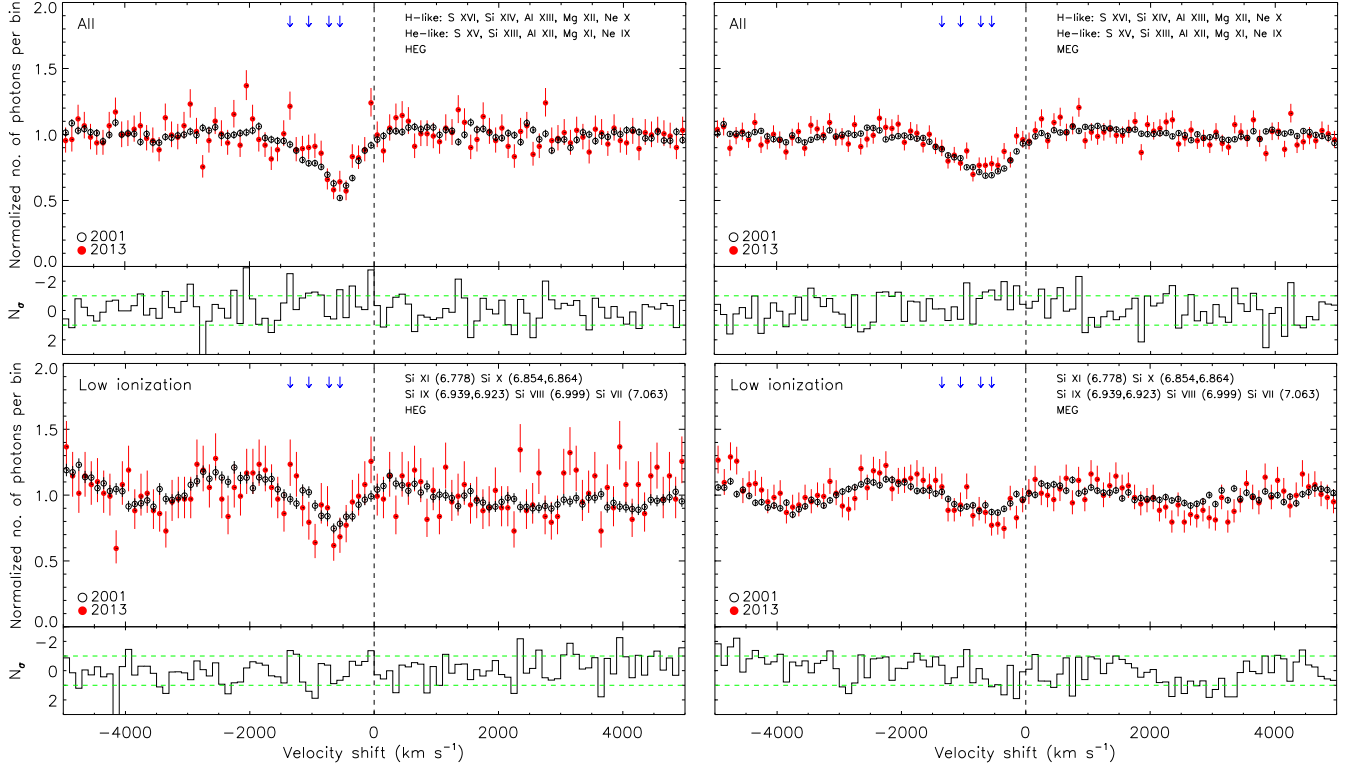


Figure 7. X-ray velocity profiles. Top - velocity spectra created by stacking all 23 absorption lines due to H- and He-like S, Si, Al, Mg, and Ne into the same profile. Bottom - velocity spectra created from *only* absorption lines due to lower ionization states of Si (Be-like, B-like, C-like, N-like, and O-like). Colors and symbols are the same as in Figure 6. HEG profiles are shown on the left, MEG on the right.

Table 4
Gaussian fitting results for the X-ray velocity profiles

Element	Species	Arm	σ_{inst} (km s^{-1})	2001				2013				Consistent $v_{\text{shift}}?$	
				v_{shift} (km s^{-1})	σ_{obs} (km s^{-1})	Resolved?	σ_{true} (km s^{-1})	v_{shift} (fixed) (km s^{-1})	v_{shift} (km s^{-1})	σ_{obs} (km s^{-1})	Resolved?		σ_{true} (km s^{-1})
S	H, He	HEG	383	-653 ± 65	376 ± 66	×	N/A	-571 ± 200	0.4σ
	H, He	MEG	734	-966 ± 73	525 ± 75	×	N/A	-847 ± 229	0.5σ
Si	H, He	HEG	309	-603 ± 19	412 ± 20	✓	273	-630 ± 75	-610 ± 61	311 ± 63	×	N/A	0.3σ (0.1σ)
	H, He	MEG	592	-718 ± 19	525 ± 20	×	N/A	-757 ± 69	-758 ± 71	530 ± 74	×	N/A	0.5σ (0.5σ)
	Low	HEG	225	-597 ± 28	224 ± 28	×	N/A	-697 ± 104	-711 ± 87	251 ± 91	×	N/A	0.9σ (1.2σ)
	Low	MEG	432	-661 ± 40	322 ± 41	×	N/A	...	-488 ± 70	250 ± 70	×	N/A	(2.1σ)
Al	H, He	HEG	266	-536 ± 22	78 ± 20	×	N/A	-510 ± 67	0.4σ
	H, He	MEG	510	-544 ± 67	261 ± 68	×	N/A	-877 ± 262	1.2σ
Mg	H, He	HEG	215	-587 ± 19	297 ± 19	✓	205	-630 ± 79	-613 ± 50	179 ± 52	×	N/A	0.5σ (0.5σ)
	H, He	MEG	412	-596 ± 21	395 ± 21	×	N/A	-773 ± 81	-759 ± 99	352 ± 101	×	N/A	2.1σ (1.6σ)
Ne	H, He	HEG	157	-727 ± 25	406 ± 28	✓	374
	H, He	MEG	301	-734 ± 18	380 ± 19	✓	231	-947 ± 99	-948 ± 138	379 ± 153	×	N/A	2.1σ (1.5σ)
All	H, He	HEG	383	-612 ± 13	345 ± 13	×	N/A	-603 ± 47	-582 ± 34	220 ± 34	×	N/A	0.2σ (0.8σ)
	H, He	MEG	734	-686 ± 13	429 ± 13	×	N/A	-782 ± 45	-779 ± 53	413 ± 54	×	N/A	2.0σ (1.7σ)

Notes. σ_{inst} is the instrumental resolution for the shortest wavelength line included in the stack. Blank entries indicate no good Gaussian fit was obtained. In the case of Ne, this is because the 2013 HEG velocity profile contains only ~ 5 counts per bin. The final column lists whether the velocity shifts measured for each profile are consistent between the two epochs. Values quoted are the significance of differences between the fit to the 2001 data and the fixed profile fit to the 2013 data. Where possible, a comparison with a free profile fit is listed in parentheses. ‘Low’ indicates the best-fitting results to the Si profiles constructed from low-ionization absorption lines only, rather than those from H- and He-like ions.

tion, using a χ^2 minimization technique. We model the 2001 data with both the centroid, v_{shift} , and width, σ_{obs} , of the Gaussian as free parameters. Where possible, we also leave these parameters free to vary in the fit to the 2013 data but we also fix the width of the Gaussian to that determined in the 2001 data and allow only the centroid to vary. For a velocity profile to be resolved, it must be broader than σ_{inst} i.e., $\sigma_{\text{obs}} - \Delta\sigma_{\text{obs}} > \sigma_{\text{inst}}$ where $\Delta\sigma_{\text{obs}}$ is the error on σ_{obs} . In cases where this is true, the intrinsic width of the profile is determined from $\sigma_{\text{true}}^2 = \sigma_{\text{obs}}^2 - \sigma_{\text{inst}}^2$. The best-fitting Gaussian parameters from this modeling, along with the instrumental resolutions for each profile, and an indication of whether a particular profile is resolved or not, are listed in Table 4. The final column of this table lists whether the velocity profiles have a consistent velocity shift between the two epochs. This is determined based on the values from the fixed shape profile fits to the 2013 data; if a free fit was possible this value is also quoted in parentheses. These values are all $\leq 2.1\sigma$ showing that in general, the X-ray outflow velocities are consistent in each epoch and there are no significant changes in the kinematic structure of the absorbing material. Profiles showing the highest significance changes in velocity shift include the MEG profile of H- and He-like Mg which shows a slight shift toward a larger outflow velocity in 2013, however, in this case (and many others) the profile for neither epoch is instrumentally resolved and the velocity shifts obtained using the HEG profiles are consistent. The MEG profile of Ne only includes ~ 14 counts per bin in the 2013 spectrum, resulting in a poorly defined profile. The MEG velocity profile produced from all 23 H- and He-like absorption lines of S, Si, Al, Mg, and Ne shows a change in the velocity shift between epochs with a significance of $\sim 2\sigma$, but again, the HEG profiles have consistent velocities. With 10 profiles being considered, we might expect to detect a velocity shift with $> 2\sigma$ significance in at least one case.

The weighted average velocity shift of the profiles listed in Table 4 (H- and He-like only) is $v = -647 \pm 22 \text{ km s}^{-1}$ in 2001 and $v = -672 \pm 66 \text{ km s}^{-1}$ in 2013, which are consistent with each other. The average velocity shift for 2013 from the fixed-profile fits is also consistent, although it does have a larger error; $-688 \pm 87 \text{ km s}^{-1}$. These values also agree with the average velocity shifts determined from the individual lines as listed in Table 3; $v = -654 \pm 14 \text{ km s}^{-1}$ (2001), $v = -693 \pm 58 \text{ km s}^{-1}$ (2013). The average widths of the velocity profiles are also consistent, $\sigma_{\text{obs}} = 352 \pm 22 \text{ km s}^{-1}$ in 2001 and $\sigma_{\text{obs}} = 309 \pm 69 \text{ km s}^{-1}$ in 2013, although none of the profiles in the 2013 data are actually resolved. The asymmetry of the profiles observed by K02, possibly as a result of another absorption system with a higher outflow velocity, is not apparent in the less well defined 2013 profiles. This justifies the use of a single Gaussian in our fitting, which although perhaps not strictly representative of the profile, allows us to make simple comparisons between the two epochs.

In the case of Si we are able to construct velocity profiles using lower ionization absorption lines e.g., those from Li-like ions etc (rather than H- and He-like), which may originate from different absorbing material. The best-fitting Gaussian parameters for these profiles are also listed in Table 4 (as ‘Low’), and are shown in Figure 7 (bottom). The MEG profile shows a velocity shift from $v = -661 \pm 40 \text{ km s}^{-1}$ (2001) to $v = -488 \pm 70 \text{ km s}^{-1}$ (2013) at 2.1σ significance, but neither profile is resolved.

3.3.2. UV kinematics

We also produce absorption profiles plotted in velocity space using the UV spectra. The original wavelength-binned spectra are first normalized by dividing by the estimated continuum level. This is determined from a cubic-spline fit to unabsorbed regions of the spectra on either side of absorption features, using the data binned to $\sim 0.4 \text{ \AA}$ ($\sim 0.8 \text{ \AA}$ in the case of Si) as the spline nodes. The observed wavelengths are then converted to a velocity shift with respect to the rest-frame wavelengths of the absorption lines. The resulting profiles for N V (1239 Å), C IV (1548 Å) and Si IV (1403 Å) are shown in Figure 8. Epoch 2 data are shown in black and Epoch 6 in red. The dark blue numbered arrows indicate the expected locations of the UV kinematic components based on the values previously reported by G03a; i.e., (1) -1320 km s^{-1} , (2) -548 km s^{-1} , (3) -724 km s^{-1} , and (4) -1027 km s^{-1} . In the cases of N V and C IV, the profiles created are a superposition of features due to each of the lines in the doublet. We therefore create the profile with respect to the shortest wavelength doublet member and indicate the expected locations of the kinematic components of the longer wavelength doublet member with dark blue triangles. For Si IV, the profiles from the two doublet members do not overlap. We show only the profile from the line at 1403 Å as the profile from the shorter wavelength line contains a strong Galactic absorption feature. Blue cyan stars on each figure indicate the location of such interstellar features. The right hand plots in Figure 8 show a smoothed version of each velocity profile, produced by a cubic spline fit to the data binned to $5\times$ the original velocity bin size.

In all three of the UV absorption profiles, kinematic component 1, which was very strong in Epoch 2 (2001) has completely disappeared by Epoch 6 (2013). Similarly, component 4, which was not present in Epoch 2, appears in all three profiles in Epoch 6. While this may simply be due to the strengthening and weakening of physically distinct absorption components, G03b reported a deceleration of component 1. Quoted on Figure 8 are the velocity shifts measured from the minima of the absorption troughs and the inferred decelerations, assuming these remain constant over the full 12 yr period. We find a velocity shift of $\Delta v_r \sim -268 \text{ km s}^{-1}$ corresponding to a deceleration of $a_r \sim 7 \times 10^{-7} \text{ km s}^{-2}$. This is lower than the average deceleration reported by G03b, but they did find a change in the deceleration within their observations ($a_r \sim 8 \times 10^{-7} \text{ km s}^{-2}$ between Epochs 1 \rightarrow 2 and $a_r \sim 18 \times 10^{-7} \text{ km s}^{-2}$ between 2 \rightarrow 3). The apparent depth of the absorption trough now at component 4 is similar to that which was at component 1, supporting the idea that it may be due to the same physical absorption component. However, the profile shape appears strongly asymmetric in Epoch 6 and the N V profile suggests this may be due to a superposition of two separate components. While this could be due to the sub-components of component 1 having different decelerations, the asymmetry is also clearly observed in the Si IV profile which is not expected to be the case in such a scenario. This will be discussed further in J. Gabel et al. (in preparation).

The N V and C IV profiles both show a strong velocity component 3 in their Epoch 2 spectra, which is weak, or even no longer present in Epoch 6. Similarly, component 2 is weak in Epoch 2, but strong in Epoch 6. Component 2 is also weakly present in the Si IV profile in Epoch 6. In the case of C IV, component 4 from the longer-wavelength member of the doublet is expected to appear at the same outflow velocity

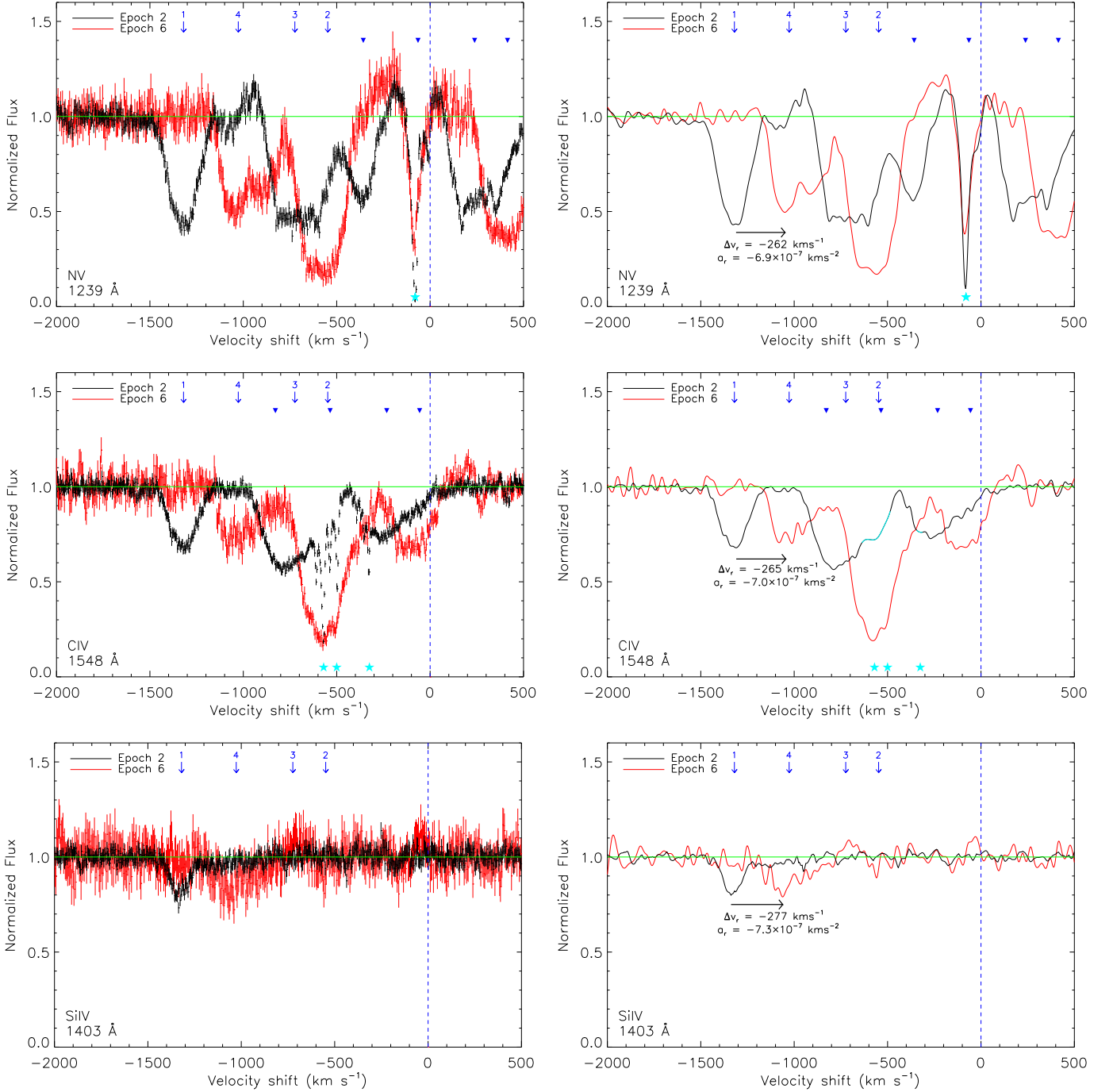


Figure 8. Velocity profiles for the UV absorption lines N V (top), C IV (middle), and Si IV (bottom). They are created after first dividing by the continuum level, estimated with a cubic spline fit to unabsorbed regions either side of the lines, before converting the observed wavelength to a velocity blueshift with respect to the rest-frame wavelength of the lines. Epoch 2 data (2001) are shown in black, Epoch 6 data (2013) are shown in red. The velocity bin size is 4–5 km s⁻¹ for the left-hand plots. Dark blue arrows indicate the locations of the UV kinematic components using values from G03a. In the case of N V and C IV, the profile includes features from both doublet members. In these cases, the expected location of the components from the longer wavelength line are marked with the dark blue triangles. Cyan stars indicate the locations of interstellar absorption lines. Right hand panels show the same velocity profiles, but with a cubic spline fitted to the data with the binning increased to 5× the original. In the case of C IV, the ISM absorption lines in the Epoch 2 data have been excluded from the spline fit; these portions are highlighted in cyan. The velocity shifts and decelerations quoted on each figure are determined from the minima of the absorption troughs assuming the physical absorption component originally at the velocity shift of component 1 has decelerated at a constant rate to the velocity shift of component 4.

as component 2, possibly distorting the profile, but the N v profile which shows similar general effects, suffers from no such contamination. These observations may again be due to the independent strengthening and weakening of different absorption components, particularly as the two absorption profiles show different shapes, the one in Epoch 6 being both narrower and deeper; however the total area of each remains similar. This may suggest that component 3 has decelerated to the velocity shift of component 2. No deceleration of this component was found in the initial study by G03b, but the deceleration implied would be $a_r \sim 3.3 \times 10^{-7} \text{ km s}^{-2}$, corresponding to a velocity change of only $\Delta v_r = -19 \text{ km s}^{-1}$ between Epochs 1 and 3 investigated by G03b. Such a shift would not have been detected due to the wide absorption trough of this component ($\sim 200 \text{ km s}^{-1}$).

3.4. X-ray/UV absorber connection

The UV velocity profiles indicate significant changes in the 12 yr period between the observations, possibly due to radial deceleration of the absorbing material. Such changes are not apparent in the X-ray velocity profiles; the broad profile shapes remain similar between epochs and no velocity shifts are detected significant at $> 3\sigma$. The possible velocity shifts in the UV are $\Delta v_{r,1 \rightarrow 4} \sim -268 \text{ km s}^{-1}$ and $\Delta v_{r,3 \rightarrow 2} \sim -125 \text{ km s}^{-1}$. Although the typical errors in the X-ray velocity estimates are only $50\text{--}100 \text{ km s}^{-1}$, the widths of the profiles are very broad, $\sigma_{\text{obs}} > 300 \text{ km s}^{-1}$ in each epoch, and few are instrumentally resolved. Therefore it is unlikely that velocity shifts of these sizes would be detectable in the X-ray velocity profiles. Assuming typical errors on the central velocity of 40 km s^{-1} and 85 km s^{-1} on the 2001 and 2013 MEG profiles, respectively, only velocity shifts as large as $\Delta v \simeq 282 \text{ km s}^{-1}$ would be detected with 3σ significance in the X-ray data. The UV data indicate shifts smaller than this value, which are therefore unlikely to be detected in the X-ray data whether present or not.

In Figure 9 we compare the X-ray velocity profile produced from the absorption lines of H- and He-like Mg to the UV velocity profile for N v (1239 Å). We use Mg as it has one of the highest S/N X-ray profiles (along with Si), but a higher resolution (215 km s^{-1} compared with 309 km s^{-1}). We use N v as the overlap of the features from the two doublet members is lower than for C iv. While we show only one profile, the combined profiles from each of the four combinations of Mg/Si and C iv/N v, yield similar results. The top panel shows the 2001 data, with the X-ray data shown by the black open circles and the UV data shown by the smooth black curve. The UV profile has been convolved with a Gaussian of width $\sigma = 215 \text{ km s}^{-1}$, to downgrade its velocity resolution to match that of the HEG at these wavelengths (FWHM = 507 km s^{-1}). The bottom panel shows the 2013 data with red filled circles showing the X-ray data, and the red curve showing the convolved UV velocity profile. The X-ray profiles are binned using a bin size of 100 km s^{-1} as in Figures 6 and 7, which over-samples the instrumental resolution. The blue arrows indicate the locations of the four UV kinematic components identified in the 2001 data by G03a.

As seen in previous works (e.g., K02; G03a), the X-ray and UV velocity profiles appear broadly similar, suggesting that it may simply be the poorer resolution of the X-ray profile which limits our detection of relatively small kinematic changes. Figure 9 shows that the broad X-ray profile may be a superposition of all four UV kinematic components,

with the asymmetry in the 2001 X-ray profiles being due to a strong UV component 1. The small differences observed between the profiles are likely due to them probing different material. The X-ray profiles are constructed primarily of absorption lines from higher ionization state ions, whereas the UV profiles show absorption due to lower ionization state ions which may reside in different physical absorption components. However, photoionization modelling of both the 2001 X-ray and UV spectra indicates that the lowest-ionization X-ray absorber is consistent with the higher ionization UV absorbers (components 1b, 2, and 3), suggesting a physical connection between at least some of the X-ray and UV absorbing material (Netzer et al. 2003; Gabel et al. 2005).

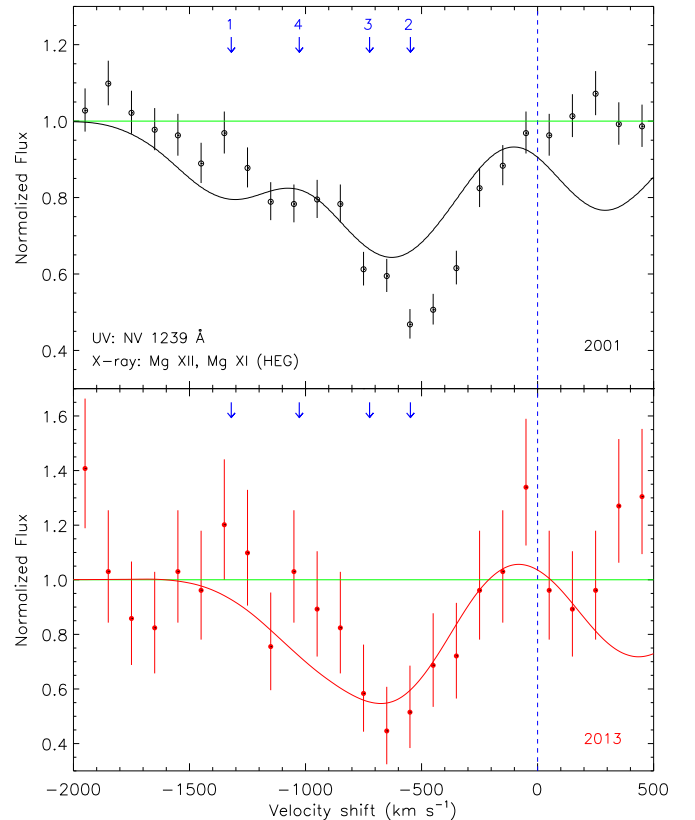


Figure 9. A combined X-ray and UV velocity profile. The top panel shows the data from 2001; black, open circles are the X-ray velocity profile constructed from absorption lines of H- and He-like Mg (Mg XII and Mg XI) detected in the HEG. The smooth black curve represents the UV velocity profile from the absorption line N v at 1239 Å which has been convolved with a Gaussian of width $\sigma = 215 \text{ km s}^{-1}$ in order to downgrade the spectrum to match the velocity resolution of the HEG at these wavelengths ($\sim 7.1 \text{ Å}$). Note that the dip in the UV profile at $v > 0 \text{ km s}^{-1}$ is due to the longer wavelength doublet member of N v at 1243 Å. The bottom panel considers the data from 2013, where the UV profile is indicated by the smooth red curve and the X-ray profile is shown by the red, filled circles and 1σ error bars. The X-ray velocity profiles are binned using a bin width of 100 km s^{-1} , although we note that this over-samples the velocity resolution. The blue arrows in each panel indicate the location of the four UV kinematic components using the values quoted in G03a. Note that the two panels have different y-axis ranges.

3.5. Iron K region

In this section, we investigate possible changes in the iron K region of the spectra between the two epochs.

A relativistically broadened iron $K\alpha$ emission line at 6.4 keV has been detected in observations of NGC 3783 by

ASCA (Nandra et al. 1997), *BeppoSAX* (De Rosa et al. 2002), *Suzaku* (Brenneman et al. 2011), and *XMM-Newton* (Blustin et al. 2002), although analysis of the *XMM-Newton* spectrum by Reeves et al. (2004) showed that when the warm absorbers were thoroughly modelled in the spectra, the requirement for a relativistic iron line was greatly reduced. The *Chandra* data also did not require a broad line in the modelling, showing only a narrow core likely produced in distant material (Kaspi et al. 2002). However, analysis by Yaqoob et al. (2005) found that the excess of emission at the base of the line could be well described by either a Compton-scattering ‘shoulder’ or with a disk-line model. A weaker emission line due to a blend of Fe $K\beta$ and Fe XXVI emission has been detected in previous observations (Blustin et al. 2002; Kaspi et al. 2002; Reeves et al. 2004; Yaqoob et al. 2005; Brenneman et al. 2011), although due to the low branching ratio (150:17 between the $K\alpha$ and $K\beta$ transitions), this feature is unlikely to be significantly detected in the *Chandra* HEG data (2001 or 2013). An absorption line due to highly ionized iron has been detected in *Chandra* and *Suzaku* observations (Kaspi et al. 2002; Yaqoob et al. 2005; Brenneman et al. 2011) and *XMM-Newton* observations showed it to be variable on timescales of $\sim 10^5$ s (Reeves et al. 2004). The depth of the line varied from one orbit to the next, appearing strongest when the continuum flux was higher. It is likely due to the highest ionization component of the warm absorber ($\log \xi \sim 3$, $N_{\text{H}} = 5 \times 10^{22} \text{ cm}^{-2}$) located within 0.1 pc of the nucleus, passing across the central X-ray emitting source (Reeves et al. 2004).

For our analysis, only data from the HEG were used, binned at 0.0025 \AA to give the highest resolution spectrum in this region. The spectral modelling was done in XSPEC v12.7.1, using the C -statistic (Cash 1979). Figure 10 shows the ratio of the data to a simple power-law model fit over the energy range 5.0–7.5 keV (1.6 – 2.5 \AA), excluding 6.0–6.5 keV. Black corresponds to the 2001 data, red shows the 2013 data, and the binning in each data set has been increased in the figure for clarity. The power-law indices were initially left free to vary independently, but were found to be consistent within their 90% errors and were subsequently tied to the same value. The normalizations remain free to vary independently. Although the warm absorbers may introduce subtle spectral curvature (Reeves et al. 2004; Patrick et al. 2011) which is not taken into account by our simple modelling of the continuum, this should not significantly impact our primary goal of comparing the two data sets obtained at different epochs.

Figure 10 clearly shows the iron $K\alpha$ emission-line in both epochs. We therefore fit a power-law plus Gaussian emission line model, $\text{phabs} * (\text{po} + \text{zgauss})$ in XSPEC, to data in the energy range 5–7.5 keV. We continue to use the Cash statistic, and errors on best-fitting spectral parameters are quoted at 90% significance. The best-fitting power-law slopes over this range are consistent in each epoch, as are the best-fitting parameters of the iron $K\alpha$ emission line, which are listed in Table 5. The addition of the Gaussian emission-line to a simple power-law model over this energy range results in an improvement in the Cash statistic of $\Delta C = 732$ in 2001 and $\Delta C = 145$ in 2013, with $C = 367$ in 2001 and $C = 350$ in 2013, for 324 degrees of freedom (ν). The EW of the line does not change significantly between epochs and is consistent with literature values (Kaspi et al. 2002; Reeves et al. 2004; Yaqoob et al. 2005). Although the underlying continuum flux in the 5–7.5 keV energy range drops significantly in the 2013 data, the line flux remains consistent between epochs. The width of the line is also consistent for each epoch and

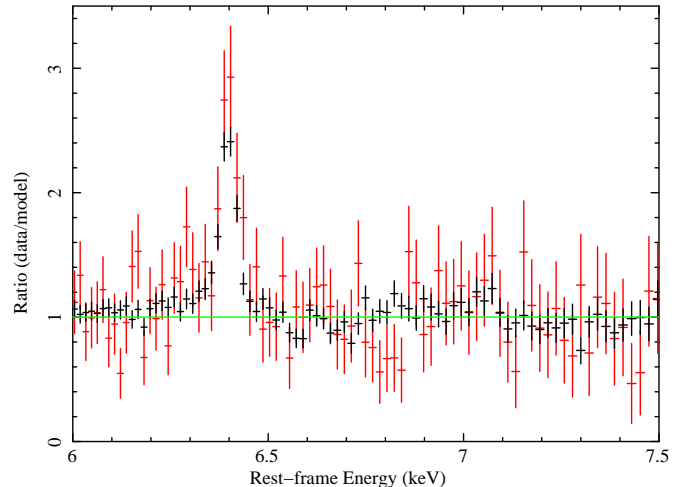


Figure 10. The iron $K\alpha$ emission-line region of NGC 3783. Shown is the ratio of the HEG data to a power-law model fit over the energies 5–6 and 6.5–7.5 keV. This simple model is used here for illustrative purposes only. The data from 2001 are shown in black and the 2013 data are shown in red. The spectra from both epochs are modelled simultaneously, with Γ tied to a common value, but the normalizations allowed to vary independently. The data has been displayed with an increased binning for clarity.

corresponds to FWHM values that are slightly higher than those in the literature (Kaspi et al. 2002; Yaqoob et al. 2005), but our modelling does not take into account the Compton shoulder created at ~ 6.2 keV due to the Compton scattering of the line photons. The width is much lower than that reported by Reeves et al. (2004), although this is likely a result of the lower energy resolution of the *XMM-Newton* EPIC-pn ($\Delta E \sim 120$ eV at 6 keV; Strüder et al. 2001). The FWHM resolution of the HETGS is $\Delta E \sim 35$ eV at 6 keV, corresponding to $\sim 1750 \text{ km s}^{-1}$, and therefore the emission line is resolved in both of our data sets.

Table 5
 Iron $K\alpha$ line parameters

Parameter	2001	2013
Γ	$1.62^{+0.09}_{-0.09}$	$1.47^{+0.24}_{-0.26}$
E (keV)	$6.397^{+0.002}_{-0.003}$	$6.400^{+0.011}_{-0.010}$
σ (eV)	20^{+2}_{-4}	20^{+6}_{-11}
FWHM (km s^{-1})	2209^{+212}_{-424}	2208^{+636}_{-1413}
EW (eV)	86^{+9}_{-8}	110^{+40}_{-20}
Continuum flux ($\times 10^{-11} \text{ erg s}^{-1} \text{ cm}^{-2}$)	$1.87^{+0.03}_{-0.02}$	$1.23^{+0.06}_{-0.02}$
Line Flux ($\times 10^{-13} \text{ erg s}^{-1} \text{ cm}^{-2}$)	$6.39^{+0.49}_{-0.51}$	$5.55^{+1.03}_{-1.45}$
C/ν	367/324	350/324
ΔC	732	145

Notes. Each of these parameters are calculated from a fit to data in the 5–7.5 keV energy range. ΔC values are the improvement in the Cash statistic gained when the Gaussian is added to a simple power-law model fit to data in this energy only.

Using simple virial arguments, the distance to the material from which the iron line is emitted is 31^{+7}_{-10} light days (2001) and 31^{+14}_{-29} light days (2013), corresponding to ~ 0.026 pc. In this determination we have assumed that the material is moving entirely perpendicular to our line-of-sight and

hence assume the minimum possible velocity and thus derive a maximum radius for the location of the material. Our estimate places the material beyond the broad-line region which lies at a distance of $r = 0.0015 - 0.0018$ pc ($\text{FWHM}_{H\beta} = 2910 - 2650 \text{ km s}^{-1}$; Onken & Peterson 2002) but within the inner edge of the torus at $r_{\text{in}} = 0.061$ pc, which has been determined from near-infrared reverberation mapping (Hönig et al. 2013). Given this distance we might expect to see a response to changes in the continuum as the light travel time ($t_{\text{cross}} = 31$ days) is much shorter than the time between our observations (~ 12 yrs). However, since we likely observe a combination of emission from material at different locations around the AGN, such variations may be ‘washed out’ by the time they reach us. *RXTE* monitoring shows that the hard X-ray flux varies considerably with the largest fluctuations being $\Delta F_{2-10\text{keV}} \sim 5 \times 10^{-11} \text{ erg s}^{-1} \text{ cm}^{-2}$ on timescales of ~ 20 days. Since no *RXTE* monitoring is available after January 2012, we do not know the behavior of the continuum fluctuations immediately preceding our *Chandra* observation. We could therefore be seeing the spectrum responding to a flare in the continuum emission, an unknown time earlier. This limits our ability to put a strong constraint on variations of the iron line.

A second Gaussian emission line was included to model Fe $K\beta$ which is expected to appear in the spectrum at $E = 7.06$ keV with 11% of the Fe $K\alpha$ flux. There is a hint of this line in both data sets, but only upper limits on the EW were obtained; $\text{EW}_{2001} < 40$ eV, $\text{EW}_{2013} < 80$ eV.

A Gaussian was also added to the model to look for the variable absorption line previously reported at 6.7 keV (Reeves et al. 2004). Leaving the central energy of the line as a free parameter does not result in lines at this expected energy, particularly in the case of the 2013 data due to the potential feature at 6.8 keV, the nature of which is unclear (however we note that the bins in the 2013 spectrum contain only 10–15 counts at these energies). Constraining both the energy and width of the 6.7 keV absorption line to the parameters given by Yaqoob et al. (2005) and allowing only the normalizations to vary, we measure $\text{EW}_{2001} = 14^{+7}_{-8}$ eV and $\text{EW}_{2013} < 30$ eV. This limit is greater than the EW reported by Reeves et al. (2004) for the *XMM-Newton* orbit in which the line was strongest (17 ± 5 eV); therefore while the line may have become stronger, we cannot rule out it becoming weaker, in agreement with the observed dependence on continuum flux seen by Reeves et al. (2004).

4. SUMMARY

In this paper we have presented recent (2013) *Chandra* HETGS and *HST* COS observations of the nearby Seyfert galaxy NGC 3783 which is known to show strong absorption features in its X-ray and UV spectra. We compare these to the high-resolution, high S/N archival data from 2001, allowing us to investigate variations in the absorption over a 12 yr period. We summarize our main results below.

1. In Figure 1 we present the broadband X-ray spectra of NGC 3783 from both epochs. There is a significant drop in flux from $F_{2-6} = (3.84 \pm 0.01) \times 10^{-11} \text{ erg s}^{-1} \text{ cm}^{-2}$ in 2001, to $F_{2-6} = (2.25 \pm 0.02) \times 10^{-11} \text{ erg s}^{-1} \text{ cm}^{-2}$ in 2013. A similar ($40 \pm 4\%$) drop in the 1270–1520 Å UV flux is shown in Figure 2. The change in X-ray flux is consistent with previous variations observed by *RXTE* (see the long-term lightcurve presented in Figure 3).

2. Figure 1 also shows a significant flattening of the X-ray power-law slope from $\Gamma_{2-6} = 1.37 \pm 0.01$ in 2001, to $\Gamma_{2-6} = 1.07 \pm 0.04$ in 2013. We show that this is unlikely to be the result of an increased reflection component, although our data do not extend to the higher energies required to model this in detail. We also found no strong evidence for a large increase in the column density of the absorbing material, although smaller variations which we are unable to detect could contribute to a change in Γ . The observed variation could also simply be due to intrinsic variations within the continuum source itself.
3. Of the 19 individual absorption lines that we consider in §3.2, we find none with a significant variation in their line flux or EW between the 2001 and 2013 spectra. We therefore suggest that there are no dramatic changes in the covering factor, column density or ionization state of the absorbing material.
4. We do not find any significant change in the X-ray kinematics between the two epochs. The average outflow velocities inferred from individual absorption lines ($v_{2001, \text{lines}} = -654 \pm 14 \text{ km s}^{-1}$, $v_{2013, \text{lines}} = -693 \pm 58 \text{ km s}^{-1}$) and the average values determined from the velocity profiles (see §3.3; $v_{2001, \text{profiles}} = -647 \pm 22 \text{ km s}^{-1}$, $v_{2013, \text{profiles}} = -672 \pm 66 \text{ km s}^{-1}$) are all consistent. The widths of the velocity profiles are also consistent in each epoch; $\sigma_{\text{obs}, 2001} = 352 \pm 22 \text{ km s}^{-1}$, $\sigma_{\text{obs}, 2013} = 309 \pm 69 \text{ km s}^{-1}$.
5. We do see significant changes in the UV kinematics between the two epochs, with kinematic components 1 and 3 being much weaker in 2013, while components 4 and 2 are much stronger. This may be due to radial deceleration of the material with component 1 decelerating to the location of component 4 with $a_{1 \rightarrow 4} = 7 \times 10^{-7} \text{ km s}^{-2}$ ($\Delta v_{1 \rightarrow 4} \sim -268 \text{ km s}^{-1}$) and component 3 decelerating to the location of component 2 with $a_{3 \rightarrow 2} = 3.3 \times 10^{-7} \text{ km s}^{-2}$ ($\Delta v_{3 \rightarrow 2} \sim -125 \text{ km s}^{-1}$).
6. Despite the different behavior apparently observed in the X-ray and UV kinematics, we show that when the UV data are downgraded to the velocity resolution of the X-ray data, very similar velocity profiles are obtained. This suggests a connection between at least some of the X-ray and UV outflowing material, in agreement with previous works.
7. We detect a narrow Fe $K\alpha$ emission line at 6.4 keV in both data sets. We find no significant variation between the epochs, with the EW and flux estimates consistent within 1σ ; $\text{EW}_{2001} = 86^{+9}_{-8}$ eV, $\text{EW}_{2013} = 110^{+40}_{-20}$ eV and $F_{\text{line}, 2001} = 6.39^{+0.49}_{-0.51} \times 10^{-13} \text{ erg s}^{-1} \text{ cm}^{-2}$, $F_{\text{line}, 2013} = 5.55^{+1.03}_{-1.45} \times 10^{-13} \text{ erg s}^{-1} \text{ cm}^{-2}$. The widths of the lines are also consistent ($\text{FWHM}_{2001} = 2209^{+212}_{-424} \text{ km s}^{-1}$, $\text{FWHM}_{2013} = 2208^{+636}_{-1413} \text{ km s}^{-1}$) and using simple virial arguments, the radial distance of the material producing the iron line is found to be ~ 31 light days or 0.026 pc from the central black hole. This places the material within the inner edge of the torus but beyond the broad-line region.

In general, the physical properties of the X-ray WA in NGC 3783 appear to have remained remarkably stable between the *Chandra* HETGS observations in 2001 and 2013.

This lack of significant absorption variation suggests that the absorbers lie far from the central SMBH, consistent with previous lower limits i.e., $r \geq 3.2, 0.6, 0.2$ pc (Netzer et al. 2003) and $r \geq 2.8, 0.5$ pc (Behar et al. 2003). This places the absorbers at distances much greater than the BLR ($r = 0.0015 - 0.0018$ pc; Onken & Peterson 2002) and the inner edge of the torus ($r_{\text{in}} = 0.061$ pc; Hönig et al. 2013) and hence, taken at face value, they do not appear to be commensurate with either a disk-wind origin (Elvis 2000) or photoionization off of the inner torus edge (Krolik & Kriss 2001). However, the torus does extend to larger distances, with half-light radii of $r_{1/2} = 4.23 \pm 0.63$ pc (major axis) and $r_{1/2} = 1.42 \pm 0.21$ pc (minor axis) estimated by mid-infrared interferometry (Hönig et al. 2013), suggesting that the WA may still be related to this structure. The WA we currently observe could also have originated as a disk-wind, but travelled for many years to its current, more distant location further from the AGN. This is a scenario more consistent with that suggested by King & Pounds (2014) in which the wind collides with a shell of gas surrounding the SMBH, which rapidly slows and cools, producing an observable WA. For NGC 3783 this gas is expected to lie at $r \leq 14$ pc (determined from equation 8 of King & Pounds 2014, and using a velocity dispersion of $\sigma = 95 \pm 10$ km s⁻¹ from Onken et al. 2004), which may be too distant to explain the WA observed here, but since we only have lower limits on its distance, this cannot be stated with certainty. Netzer et al. (2003) also gave an upper limit of $r \leq 25$ pc, consistent with both this scenario, and with the expected location of the UV absorbers (Gabel et al. 2005).

While we find no statistically significant variations in the physical properties of the X-ray WA between our observations, we note that George et al. (1998) did report a decrease in the opacity by a factor of ≈ 2 over an 18 month period. This is not necessarily in conflict with our results as the observations occurred over a different time interval (1993–1996) to the data we consider here. It is also not unprecedented for AGN to show periods of stability and variability with regards to their absorption properties; e.g. NGC 5548 (Steenbrugge et al. 2005; Detmers et al. 2008; Krongold et al. 2010; Kaastra et al. 2014). This suggests that AGN can host absorbing material with a range of physical properties and distances from the central SMBH, producing variations on a wide range of timescales.

While the X-ray absorption properties lack significant variation, the UV absorbers show clear kinematic changes. However, this does not necessarily indicate that the X-ray and UV absorbing material is not physically related as we show that such changes would simply not be detected in the lower velocity resolution X-ray data. The dramatic UV variability observed on > 10 yr timescales can be reasonably expected to continue, suggesting that further monitoring of NGC 3783 in the UV is likely to yield stronger constraints on the outflow physics. The kinematic change in UV component 1 was first observed in data from 2001 but the potential deceleration of UV component 3 has required a longer baseline for detection due to its smaller magnitude. Constraining changes in this deceleration, as seen in component 1, would require an even longer baseline. Further observations would also allow more detailed discrimination between the various scenarios suggested for the deceleration; e.g. a bulk deceleration of the material or a directional shift in the motion of the absorber with respect to our line of sight.

The lack of variation seen in the X-ray WA suggests that constant monitoring will be required over many years to con-

strain fully its nature. Such a campaign is impractical with *Chandra* owing to the long required exposures; a better approach would be to trigger grating observations in response to continuous monitoring at lower spectral resolution with, e.g., *Swift*. Regular monitoring at high resolution would be an excellent and feasible program for the forthcoming *Athena* X-ray observatory.

We acknowledge the support of *Chandra* X-ray Center grant GO3-14114X, Space Telescope Science Institute grant HST-GO-13115.01-A, and NASA ADP grant NNX11AJ59G (AES, WNB). The Technion group is supported by the I-CORE program of the Planning and Budgeting Committee and the Israel Science Foundation (grant numbers 1937/12 and 1163/10), and by a grant from Israel's Ministry of Science and Technology. This work has made use of lightcurves provided by the University of California, San Diego Center for Astrophysics and Space Sciences, X-ray Group (R. E. Rothschild, A. G. Markowitz, E. S. Rivers, and B. A. McKim), obtained at <http://cass.ucsd.edu/~rxteagn/>. We also thank Ian McHardy and Phil Uttley for providing data in advance of publication, and the anonymous referee for helpful comments on the original manuscript.

Facilities: CXO (ACIS), HST (COS).

REFERENCES

- Alloin, D., Santos-Lleo, M., Peterson, B. M., et al. 1995, *A&A*, 293, 293
 Behar, E. 2009, *ApJ*, 703, 1346
 Behar, E., Rasmussen, A. P., Blustin, A. J., et al. 2003, *ApJ*, 598, 232
 Blustin, A. J., Branduardi-Raymont, G., Behar, E., et al. 2002, *A&A*, 392, 453
 Brenneman, L. W., Reynolds, C. S., Nowak, M. A., et al. 2011, *ApJ*, 736, 103
 Cash, W. 1979, *ApJ*, 228, 939
 Crenshaw, D. M., & Kraemer, S. B. 2012, *ApJ*, 753, 75
 Crenshaw, D. M., Kraemer, S. B., Boggess, A., et al. 1999, *ApJ*, 516, 750
 De Rosa, A., Piro, L., Fiore, F., et al. 2002, *A&A*, 387, 838
 de Vaucouleurs, G., de Vaucouleurs, A., Corwin, Jr., H. G., et al. 1991, Third Reference Catalogue of Bright Galaxies. Volume I: Explanations and references. Volume II: Data for galaxies between 0^h and 12^h. Volume III: Data for galaxies between 12^h and 24^h.
 den Herder, J. W., Brinkman, A. C., Kahn, S. M., et al. 2001, *A&A*, 365, L7
 Detmers, R. G., Kaastra, J. S., Costantini, E., McHardy, I. M., & Verbunt, F. 2008, *A&A*, 488, 67
 Elvis, M. 2000, *ApJ*, 545, 63
 Fabian, A. C., Kunieda, H., Inoue, S., et al. 1994, *PASJ*, 46, L59
 Ferrarese, L., & Merritt, D. 2000, *ApJ*, 539, L9
 Filiz Ak, N., Brandt, W. N., Hall, P. B., et al. 2013, *ApJ*, 777, 168
 Fruscione, A., McDowell, J. C., Allen, G. E., et al. 2006, in Society of Photo-Optical Instrumentation Engineers (SPIE) Conference Series, Vol. 6270, Society of Photo-Optical Instrumentation Engineers (SPIE) Conference Series
 Gabel, J. R., Kraemer, S. B., & Crenshaw, D. M. 2002, in Astronomical Society of the Pacific Conference Series, Vol. 255, Mass Outflow in Active Galactic Nuclei: New Perspectives, ed. D. M. Crenshaw, S. B. Kraemer, & I. M. George, 81
 Gabel, J. R., Crenshaw, D. M., Kraemer, S. B., et al. 2003a, *ApJ*, 583, 178, (G03a)
 —. 2003b, *ApJ*, 595, 120, (G03b)
 Gabel, J. R., Kraemer, S. B., Crenshaw, D. M., et al. 2005, *ApJ*, 631, 741
 Garmire, G. P., Bautz, M. W., Ford, P. G., Nousek, J. A., & Ricker, Jr., G. R. 2003, in Society of Photo-Optical Instrumentation Engineers (SPIE) Conference Series, Vol. 4851, Society of Photo-Optical Instrumentation Engineers (SPIE) Conference Series, ed. J. E. Truemper & H. D. Tananbaum, 28–44
 Gebhardt, K., Bender, R., Bower, G., et al. 2000, *ApJ*, 539, L13
 Gehrels, N. 1986, *ApJ*, 303, 336

- George, I. M., Turner, T. J., Mushotzky, R., Nandra, K., & Netzer, H. 1998, *ApJ*, 503, 174
- Gibson, R. R., & Brandt, W. N. 2012, *ApJ*, 746, 54
- Gibson, R. R., Canizares, C. R., Marshall, H. L., Young, A. J., & Lee, J. C. 2007, *ApJ*, 655, 749
- Green, J. C., Froning, C. S., Osterman, S., et al. 2012, *ApJ*, 744, 60
- Gültekin, K., Richstone, D. O., Gebhardt, K., et al. 2009, *ApJ*, 698, 198
- Halpern, J. P. 1984, *ApJ*, 281, 90
- Holczer, T., & Behar, E. 2012, *ApJ*, 747, 71
- Holczer, T., Behar, E., & Kaspi, S. 2007, *ApJ*, 663, 799
- Hönic, S. F., Kishimoto, M., Tristram, K. R. W., et al. 2013, *ApJ*, 771, 87
- Kaastra, J. S., Raassen, A. J. J., Mewe, R., et al. 2004, *A&A*, 428, 57
- Kaastra, J. S., Detmers, R. G., Mehdipour, M., et al. 2012, *A&A*, 539, A117
- Kaastra, J. S., Kriss, G. A., Cappi, M., et al. 2014, *Science*, in press
- Kaiser, M. E., Kriss, G. A., & Sembach, K. R. 2002, in *Astronomical Society of the Pacific Conference Series*, Vol. 255, *Mass Outflow in Active Galactic Nuclei: New Perspectives*, ed. D. M. Crenshaw, S. B. Kraemer, & I. M. George, 75
- Kalberla, P. M. W., Burton, W. B., Hartmann, D., et al. 2005, *A&A*, 440, 775
- Kaspi, S., Brandt, W. N., Netzer, H., et al. 2000, *ApJ*, 535, L17
- Kaspi, S., Netzer, H., Chelouche, D., et al. 2004, *ApJ*, 611, 68
- Kaspi, S., Brandt, W. N., Netzer, H., et al. 2001, *ApJ*, 554, 216
- Kaspi, S., Brandt, W. N., George, I. M., et al. 2002, *ApJ*, 574, 643, (K02)
- King, A. 2003, *ApJ*, 596, L27
- , 2005, *ApJ*, 635, L121
- King, A. R., & Pounds, K. A. 2014, *MNRAS*, 437, L81
- Kormendy, J., & Ho, L. C. 2013, *ARA&A*, 51, 511
- Kraemer, S. B., Crenshaw, D. M., & Gabel, J. R. 2001, *ApJ*, 557, 30
- Kraemer, S. B., Crenshaw, D. M., George, I. M., et al. 2002, *ApJ*, 577, 98
- Krolik, J. H., & Kriss, G. A. 2001, *ApJ*, 561, 684
- Krongold, Y., Nicastro, F., Brickhouse, N. S., et al. 2003, *ApJ*, 597, 832
- Krongold, Y., Elvis, M., Andrade-Velazquez, M., et al. 2010, *ApJ*, 710, 360
- Lamer, G., McHardy, I. M., Uttley, P., & Jahoda, K. 2003, *MNRAS*, 338, 323
- Longinotti, A. L., Krongold, Y., Kriss, G. A., et al. 2013, *ApJ*, 766, 104
- Maran, S. P., Crenshaw, D. M., Mushotzky, R. F., et al. 1996, *ApJ*, 465, 733
- Marchese, E., Braitto, V., Reeves, J. N., et al. 2014, *MNRAS*, 437, 2806
- Marinucci, A., Matt, G., Miniutti, G., et al. 2014, *ApJ*, 787, 83
- Markert, T. H., Canizares, C. R., Dewey, D., et al. 1994, in *Society of Photo-Optical Instrumentation Engineers (SPIE) Conference Series*, Vol. 2280, *Society of Photo-Optical Instrumentation Engineers (SPIE) Conference Series*, ed. O. H. Siegmund & J. V. Vallerga, 168–180
- Markowitz, A., & Edelson, R. 2004, *ApJ*, 617, 939
- Markowitz, A. G., Krumpke, M., & Nikutta, R. 2014, *MNRAS*, 439, 1403
- Mathur, S., Wilkes, B., Elvis, M., & Fiore, F. 1994, *ApJ*, 434, 493
- Matt, G., Bianchi, S., Guainazzi, M., et al. 2011, *A&A*, 533, A1
- McConnell, N. J., & Ma, C.-P. 2013, *ApJ*, 764, 184
- McKernan, B., & Yaqoob, T. 1998, *ApJ*, 501, L29
- McQuillin, R. C., & McLaughlin, D. E. 2013, *MNRAS*, 434, 1332
- Miller, L., Turner, T. J., Reeves, J. N., et al. 2007, *A&A*, 463, 131
- Miyazawa, T., Haba, Y., & Kunieda, H. 2009, *PASJ*, 61, 1331
- Mushotzky, R. F., Marshall, F. E., Boldt, E. A., Holt, S. S., & Serlemitsos, P. J. 1980, *ApJ*, 235, 377
- Nandra, K., George, I. M., Mushotzky, R. F., Turner, T. J., & Yaqoob, T. 1997, *ApJ*, 477, 602
- Nandra, K., & Pounds, K. A. 1994, *MNRAS*, 268, 405
- Netzer, H., Kaspi, S., Behar, E., et al. 2003, *ApJ*, 599, 933
- Onken, C. A., Ferrarese, L., Merritt, D., et al. 2004, *ApJ*, 615, 645
- Onken, C. A., & Peterson, B. M. 2002, *ApJ*, 572, 746
- Pan, H. C., Stewart, G. C., & Pounds, K. A. 1990, *MNRAS*, 242, 177
- Patrick, A. R., Reeves, J. N., Lobban, A. P., Porquet, D., & Markowitz, A. G. 2011, *MNRAS*, 416, 2725
- Peterson, B. M., Ferrarese, L., Gilbert, K. M., et al. 2004, *ApJ*, 613, 682
- Pounds, K. A., Reeves, J. N., Page, K. L., & O'Brien, P. T. 2004, *ApJ*, 605, 670
- Reeves, J. N., Nandra, K., George, I. M., et al. 2004, *ApJ*, 602, 648
- Reeves, J. N., Porquet, D., Braitto, V., et al. 2013, *ApJ*, 776, 99
- Reichert, G. A., Rodriguez-Pascual, P. M., Alloin, D., et al. 1994, *ApJ*, 425, 582
- Reis, R. C., Fabian, A. C., Reynolds, C. S., et al. 2012, *ApJ*, 745, 93
- Reynolds, C. S. 1997, *MNRAS*, 286, 513
- Reynolds, C. S., Brenneman, L. W., Lohfink, A. M., et al. 2012, *ApJ*, 755, 88
- Rivers, E., Markowitz, A., & Rothschild, R. 2013, *ApJ*, 772, 114
- Shields, J. C., & Hamann, F. 1997, *ApJ*, 481, 752
- Silk, J., & Rees, M. J. 1998, *A&A*, 331, L1
- Steenbrugge, K. C., Kaastra, J. S., Crenshaw, D. M., et al. 2005, *A&A*, 434, 569
- Strüder, L., Briel, U., Dennerl, K., et al. 2001, *A&A*, 365, L18
- Taylor, R. D., Uttley, P., & McHardy, I. M. 2003, *MNRAS*, 342, L31
- Tombesi, F., Cappi, M., Reeves, J. N., et al. 2013, *MNRAS*, 430, 1102
- Turner, M. J. L., Abbey, A., Arnaud, M., et al. 2001, *A&A*, 365, L27
- Turner, T. J., Kraemer, S. B., George, I. M., Reeves, J. N., & Bottorff, M. C. 2005, *ApJ*, 618, 155
- Turner, T. J., Nandra, K., George, I. M., Fabian, A. C., & Pounds, K. A. 1993, *ApJ*, 419, 127
- Turner, T. J., & Pounds, K. A. 1989, *MNRAS*, 240, 833
- Turner, T. J., Reeves, J. N., Kraemer, S. B., & Miller, L. 2008, *A&A*, 483, 161
- Vaughan, S., & Fabian, A. C. 2004, *MNRAS*, 348, 1415
- Weisskopf, M. C., Tananbaum, H. D., Van Speybroeck, L. P., & O'Dell, S. L. 2000, in *Society of Photo-Optical Instrumentation Engineers (SPIE) Conference Series*, Vol. 4012, *Society of Photo-Optical Instrumentation Engineers (SPIE) Conference Series*, ed. J. E. Truemper & B. Aschenbach, 2–16
- Willingale, R., Starling, R. L. C., Beardmore, A. P., Tanvir, N. R., & O'Brien, P. T. 2013, *MNRAS*, 431, 394
- Woodgate, B. E., Kimble, R. A., Bowers, C. W., et al. 1998, *PASP*, 110, 1183
- Yaqoob, T., Reeves, J. N., Markowitz, A., Serlemitsos, P. J., & Padmanabhan, U. 2005, *ApJ*, 627, 156